LOW-ENERGY ELECTRON INDUCED PROCESSES IN HYDROCARBON FILMS ADSORBED ON SILICON SURFACES

A Thesis
Presented to
The Academic Faculty

by

Kristin R. Shepperd

In Partial Fulfillment
of the Requirements for the Degree
Doctor of Philosophy in the
School of Chemistry and Biochemistry

Georgia Institute of Technology
August 2009

LOW-ENERGY ELECTRON INDUCED PROCESSES IN HYDROCARBON FILMS ADSORBED ON SILICON SURFACES

Approved by:

Dr. Thomas M. Orlando, Advisor
School of Chemistry and Biochemistry
Georgia Institute of Technology

Dr. W. Jack Lackey
School of Mechanical Engineering
Georgia Institute of Technology

Dr. Mostafa A. El-Sayed
School of Chemistry and Biochemistry
Georgia Institute of Technology

Dr. Laren M. Tolbert
School of Chemistry and Biochemistry
Georgia Institute of Technology

Dr. Phillip N. First
School of Physics
Georgia Institute of Technology

Date Approved: 30 June 2009

To my family,

Jerry and Maudie Shepperd, Shalli Shepperd Walker and Lisa Shepperd

ACKNOWLEDGEMENTS

The doctor of philosophy degree is generally regarded as the pinnacle of *individual* academic achievement, but this is a common misconception. A Ph. D. is most certainly not a solo effort. The work that I present in this dissertation would not and could not have been completed without the assistance of many wonderful scientists (and non-scientists) who so generously shared their knowledge with me.

First, I would like to express my sincere appreciation to my advisor, Professor Thomas Orlando. His advisement and encouragement have been invaluable in my growth as a scientist. A note of gratitude is due to my thesis committee: Dr. Mostafa El-Sayed, Dr. Phillip First, Dr. Jack Lackey, and Dr. Laren Tolbert for their assistance with the completion of this thesis. I would also like to thank the senior personnel in the Orlando lab, Dr. Alexandr Aleksandrov and Dr. Gregory Grieves. There seemed to be no technical issue they could not solve, no instrumental catastrophe they could not avert, and no fundamental scientific question they could not answer. I am truly grateful to Greg and Alex for all of their advisement and instruction. Furthermore, I would like to thank all of my fellow group members, who have been constant sources of friendship, laughter, advice, and commiseration. Past and present labmates include: Dr. Janine Captain, Dr. Haiyan Chen, Dr. Yanfeng Chen, Dr. Christopher Lane, Dr. Doogie Oh, Dr. Taishan Fan, Dr. Jason McLain, Babajide Olanrewaju, Irene Anestis-Richard, Denis Sokolov, Michele Dawley, Michael Poston, Marcus Johnson, Joshua Symonds, Hannah Barks, Kenneth Kite, Lan Sun, Alice Johnson, and Torri Rose. I am particularly indebted to Christopher Lane, who, from my first day in the lab, took me under his wing and really showed me the ropes. The REMPI work would have been impossible without his help. I thank Denis Sokolov

for all of his assistance with the graphene oxide project. Also, I am very appreciative to the scientists with whom I have collaborated, particularly Professor Phillip First and his students, Dr. Tianbo Li, Dr. Joanna Hass and Dr. Nikhil Sharma.

Finally, none of this would have been possible without my family and friends. Much appreciation goes to my good friends Carla Winnubst and Dr. Paul Newhouse. I could always depend on Carla for a sympathetic ear and her professional psychological advice. And I will always remember the many transcontinental commiseration/encouragement sessions via telephone with Paul. I thank my parents, Jerry and Maudie Shepperd for their constant love, unwavering support and encouraging words. Many thanks go to my sister, Shalli, for always being in my corner and for patiently and sympathetically listening to my vents about the frustrations of graduate school. Most of all, I thank my little sister, Lisa. Lisa is the odds defy-er, the never-say-die-er; and her strength, courage, and perseverance have inspired me more than she will ever know.

TABLE OF CONTENTS

DEDICATION iii

ACKNOWLEDGEMENTS iv

LIST OF TABLES ix

LIST OF FIGURES x

SUMMARY xiv

I INTRODUCTION 1

1.1 Low-Energy Electron Collisions with Surfaces 1

1.1.1 Inelastic Scattering of Low-Energy Electrons 1

1.1.2 Dissociative Electron Attachment 3

1.2 Electron-Stimulated Desorption 4

1.3 Electron Beam Chemical Vapor Deposition 7

1.4 Overview 9

II ELECTRON BEAM CHEMICAL VAPOR DEPOSITION OF CARBON ON SILICON(111) FROM AN ACETYLENE PRECURSOR 11

2.1 Introduction 11

2.2 Experimental Details 14

2.3 Results 15

2.3.1 Scanning Electron Microscopy Images 15

2.3.2 Auger Electron Spectra 16

2.4 Discussion 18

2.4.1 Analysis of Carbon KLL Auger Spectra 18

2.4.2 Effect of Low-Energy Electron Bombardment 19

III ACETYLENE ADSORBED ON THE SILICON(111) SURFACE 21

3.1 Introduction 21

3.2 Bonding Geometry and Saturation Coverage 21

3.2.1 The Si(111)-(7×7) Surface 21

3.2.2 Acetylene Adsorption on the Si(111)-(7×7) Surface 24
3.3 Electronic Structure 26
IV ELECTRON-STIMULATED DESORPTION OF CATIONS FROM DEUTERATED ACETYLENE ADSORBED ON THE SILICON(111) SURFACE 30
4.1 Introduction 30
4.2 Experimental Details 30
4.3 Results 33
4.3.1 Threshold Data 33
4.4 Discussion 35
4.4.1 D^+ Appearance Threshold 35
4.4.2 $C_2D_2{}^+$ Threshold 36
4.4.3 Resonance Structure in the $C_2D_2{}^+$ Spectrum 38
4.4.4 Threshold Energies of Hydrocarbon Fragments 39
4.5 Conclusions 39
V ELECTRON-STIMULATED DESORPTION OF ATOMIC DEUTERIUM FROM DEUTERATED ACETYLENE ADSORBED ON THE SILICON(111) SURFACE 41
5.1 Introduction 41
5.2 Experimental Details 42
5.3 Results 43
5.3.1 Incident Electron Energy Dependence 43
5.3.2 Time-of-Flight Distributions 44
5.4 Discussion 46
5.4.1 Appearance Threshold at 8 eV 46
5.4.2 Structure at 13–14 eV 47
5.4.3 The $D(^2S)$ Energy Distribution 48
5.5 Conclusions 51
VI LOW-ENERGY ELECTRON INTERACTIONS WITH EPITAXIAL GRAPHENE ON SILICON CARBIDE (0001) 52
6.1 Introduction 52

6.2 Experimental Details 54
6.3 Results 54
6.3.1 Electron-Stimulated Desorption of Cations from Epitaxial Graphene on SiC(0001) 54
6.3.2 Cation Desorption Yields as a Function of Electron Fluence 57
6.4 Discussion 58
6.4.1 Appearance Threshold Energies of Cations 58
6.4.2 Behavior of Cations as a Function of Electron Fluence . . . 59
6.5 Conclusions 60
VII LOW-ENERGY ELECTRON INTERACTIONS WITH GRAPHENE OXIDE FILMS ON SILICON(100) 61
7.1 Introduction 61
7.2 Experimental Details 63
7.3 Results 65
7.3.1 Electron-Stimulated Desorption of Cations from Graphene Oxide on Si(100) 65
7.3.2 Cation Desorption Yields as a Function of Electron Fluence 68
7.3.3 Auger Electron Spectra of Pre- and Post-irradiated Graphene Oxide Films 69
7.4 Discussion 70
7.4.1 Appearance Threshold Energies of Cations 70
7.4.2 Behavior of Cations as a Function of Electron Fluence . . . 71
7.5 Conclusions 72
VIII CONCLUSION 74
REFERENCES 77

LIST OF TABLES

3.1 The seven possible Si atom pairs of the Si(111)-(7×7) surface and the corresponding Si–Si distance. Adapted from Ref. 52. 25

3.2 Ionization potentials of the occupied molecular orbitals of gaseous and condensed acetylene [58, 59]. 26

6.1 Removal cross sections for selected cations emitted from ESD of epitaxial graphene on SiC(0001) at 50 eV. 60

7.1 Removal cross sections for cations emitted from ESD of graphene oxide deposited on Si(100) at 50 eV. 72

LIST OF FIGURES

1.1 a) Possible pathways produced from an electron collision with target molecule AB. b) Dissociation and energy dissipation pathways of the transient negative ion (TNI) created via electron attachment to AB [13]. 2

1.2 Schematic potential energy curves for the interaction between a surface, M and an atom, A. Panel a) illustrates desorption of an ion, A^+ and b) depicts neutral desorption. $E_d(A)$ is the binding energy of the atom to the surface, and $E_i(A)$ is the ionization potential of the atom [20–22]. 6

1.3 Schematic illustrating the electron-beam-induced deposition (EBID) process. 8

2.1 Schematic illustrating the Auger process. 14

2.2 The custom-built EBCVD ultrahigh vacuum chamber. 15

2.3 SEM images of carbon films deposited on Si(111) via a) conventional CVD and b) EBCVD. 16

2.4 Auger electron spectra of the Si(111) surface following CVD (blue curve) and EBCVD (red curve) using an acetylene precursor. 17

3.1 The DAS model of the Si(111)-(7×7) surface (adapted from Ref. 51). In the top view, the gray dashed line outlines the unit cell. The different types of silicon atoms are shown in the top and side views. Dimers are represented as green circles, rest atoms are shown as blue circles and adatoms are red circles. 23

3.2 Schematic of an acetylene molecule di-σ bonded across two adjacent Si atoms of the Si(111)-(7×7) surface (adapted from Ref. 52 and 53). Silicon atoms are represented as gray spheres, carbon atoms as blue spheres and hydrogen atoms as red spheres. 24

3.3 Electronic structure diagram of acetylene di-σ bonded to the Si(111)-(7×7) surface [50, 57, 61]. The antibonding electrons of the $(\pi\text{–R})^*$ state (enclosed in the blue circle) are donated into the $(\pi\text{–AD})^*$ state, as indicated by the dashed arrow, giving the Si(111)-(7×7):C_2H_2 system bonding character. 28

3.4 Schematic of the energy level diagram of clean Si(111)-(7×7) and acetylene referenced to the Fermi level. The values on the left are compiled from UPS data from Fock, et al. [59] and Rowe, et al. [62]. The Si(111)-(7×7) UPS data was traced from Rowe, et al. [62]. 29

4.1 Illustration of the UHV chamber where the ESD experiments were performed. 32

4.2 Diagram of the ESD-TOF-MS experiment with the pulse sequence used for detection of the cations. 32

4.3 Typical TOF-MS of cations emitted from ESD of C_2D_2 adsorbed on Si(111)-(7×7) at 50 eV. The high mass fragments are multiplied by a factor of 5 for ease of comparison. The assignments for the peaks labeled a–f are: a) $C_2D_2^+$, b) C_2HD^+, c) C_2D^+ (or possibly $C_2H_2^+$), d) C_2^+, e) H_3O^+, and f) CD^+. 33

4.4 The top frame displays the yields of D^+ (filled circles) and $C_2D_2^+$ (open circles) from the ESD of acetylene-d_2 adsorbed on Si(111)-(7×7) as a function of incident electron energy. The $C_2D_2^+$ curve is multiplied by a factor of 5 to facilitate comparison of the ion yield curve shapes. The bottom frame presents the yields of the acetylene fragments CD^+ (filled triangles) and C_2D^+ (open triangles). All data has been normalized to the electron beam current. 34

4.5 Illustration of the desorption mechanism of D^+ from ESD of acetylene adsorbed on Si(111)-(7×7). Step 1 depicts the initial excitation of the C 2s (or 2σg) level of the acetylene molecule by the incident electron. Step 2 shows Auger decay of an electron from a shallow level into the C 2s. Step 3 shows the ejection of the Auger electron, resulting in two holes localized at the shallow level. 36

4.6 Schematic of the desorption mechanism of $C_2D_2^+$ from ESD of acetylene adsorbed on Si(111)-(7×7) due to Auger decay. Bombardment of the complex with 12–13 eV electrons results in the ejection of an electron localized in the π–R level. Auger cascade occurs as an electron from the π^*–AD level fills the hole, causing ejection of the other electron in the π^*–AD level. The two-hole state Coulomb explodes, leading to desorption of $C_2D_2^+$. 38

5.1 (2 + 1) REMPI detection scheme used for atomic deuterium D(^{2}S) from the ESD of acetylene-d_2 adsorbed on Si(111)-(7×7). 42

5.2 Diagram of the ESD-REMPI-TOF experiment with the pulse sequence used for detection of the neutral desorbates. 43

5.3 Plot of the neutral D(^{2}S) yield versus incident electron energy. The data was obtained by probing the D($3s\ ^2\mathrm{S} \leftarrow 1s\ ^2\mathrm{S}$) REMPI transition. The inset shows the low energy region of the spectrum. Error bars of selected data points verify the structure in the intensity. 44

5.4 Summation of multiple Maxwell-Boltzmann distributions (solid line) fit to D(^{2}S) time-of-flight data taken at 50 eV. The dotted line represents the thermal Maxwell-Boltzmann distribution with an effective temperature of 130 K. The dashed and dashed/dotted lines represent a highly energetic non-thermal component and a non-thermal intermediate component, respectively. 46

5.5 Schematic illustrating the probable desorption trajectories of deuterium atoms ejected from di-σ bonded acetylene on the Si(111)-(7×7) surface. The distance from the surface normal to the laser field is 4.0 mm. Deuterium atom 1 (on the left) is 25° off the surface normal, resulting in a distance, d_1, of 4.4 mm to the laser field. For deuterium atom 2 (on the right), the 65° offset from the surface normal results in a distance, d_2 of 9.5 mm to the laser field. 50

6.1 Structures of the sp^2 hybridized allotropes of carbon. 53

6.2 A typical ESD-TOF mass spectrum of cations emitted from epitaxial graphene on SiC(0001) from bombardment with 50 eV electrons. The higher mass peaks are multiplied by a factor of five for ease of comparison. 55

6.3 Cation yields produced from ESD of epitaxial graphene as a function of incident electron energy. In frame a) H^+, b) CH_3^+, and c) $C_3H_x^+$ (filled circles) and $C_5H_x^+$ (empty circles). Each data point is representative of the corresponding mass peak area. Data are normalized to the electron beam current. 56

6.4 The yields of H^+ (black circles), CH_3^+ (red circles), $C_3H_x^+$ (green circles) and $C_5H_x^+$ (blue circles) plotted as a function of electron dose. The CH_3^+, $C_3H_x^+$, and $C_5H_x^+$ data were normalized to the H^+ intensity at t = 0. 57

7.1 Structural model of graphite oxide [109]. 62

7.2 a) AFM and b) SEM images of graphene oxide flakes deposited on Si(100). The preparation of the graphene oxide samples and acquisition of the AFM and SEM images by Denis Sokolov, GIT. 64

7.3 A typical ESD-TOF mass spectrum of cations emitted from graphene oxide deposited on Si(100) under the irradiation of 50 eV electrons. . 65

7.4 ESD cation yields as a function of incident electron energy. Each data point is representative of the corresponding mass peak area. The data are normalized to the electron beam current. 67

7.5 The yields of H^+ (black circles), HCO^+ (red circles), $HCCO^+$ (green circles) and $C_2H_3^+$ (blue circles) as a function of electron dose. The HCO^+, $HCCO^+$, and $C_2H_3^+$ data were normalized to the H^+ signal intensity at t = 0. 68

7.6 Auger spectra of graphene oxide deposited on Si(100) before (blue curve) and after (red curve) bombardment with 50 eV electrons (total fluence $\sim 20 \times 10^{18}$ cm^{-2}). The inset shows the C KLL region. 69

SUMMARY

The deposition of hydrocarbons on silicon substrates is a topic of wide interest. This is generally related to the technological importance of silicon carbide (SiC) and a growing interest in graphene and graphitic materials [1, 2]. Methods for producing these materials predominantly involve high processing temperatures. In the case of SiC, these high processing temperatures often result in the formation of surface defects, which compromise the electronic properties of the material [3–6]. In an effort to grow SiC films at low temperatures, a technique known as electron-beam chemical vapor deposition (EBCVD) has been developed. Most electron beam deposition techniques employ a focused beam of high-energy (20–30 keV) electrons to form nanometer-sized solid deposits on a surface [7–11]. However, in an effort to deposit macroscale films, a broad beam of low-energy electrons was used [12].

In addition to investigating the applications of low-energy electrons in semiconductor film growth, the fundamental chemical and physical processes induced by the bombardment of adsorbate-covered surfaces with low-energy electrons were examined. Specifically, Chapters 2–5 discuss studies which explore the adsorption of acetylene on a Si(111)-(7×7) surface. These investigations demonstrate the utility of low-energy electron irradiation in the removal of hydrogen from chemisorbed acetylene. Electron-stimulated desorption measurements show that protons, as well as neutral hydrogen species, are removed by the interaction of incident electrons with very low kinetic energies. Further evidence of dehydrogenation is confirmed by the appearance of graphitic features in the Auger electron spectrum of the post-irradiated acetylene film. Chapters 4 and 5 describe in detail the mechanisms governing the low-energy electron-induced desorption of hydrogen and other fragments produced from

the acetylene:Si(111)-(7×7) adsorbate-substrate system. The effects of low-energy electron collisions with extended graphitic networks are outlined in Chapters 6 and 7. Epitaxial graphene grown on SiC(0001) is the focus of Chapter 6. Species produced and emitted as a result of electron-stimulated desorption are measured as a function of incident electron energy and the excitations responsible for their creation and desorption are discussed. In Chapter 7, low-energy electron interactions with graphene oxide thin films deposited on a Si(100) single crystal are discussed. The yields of positively charged species desorbed from the surface are analyzed and the mechanisms governing their formation and removal are proposed. Additionally, the effects of prolonged electron beam irradiation of the surfaces of epitaxial graphene and graphene oxide were explored.

CHAPTER I

INTRODUCTION

The interaction of low-energy electrons with polyatomic collision partners is a topic of scientific and technological significance. These collision events are prevalent in nature and are ubiquitous in plasma and high-energy electron processing techniques used in the device industry. In the latter case, a focused beam of high-energy ($\sim$ 20–30 keV) electrons can also be used to induce the growth of nanoscale features in a process known as electron-beam chemical vapor deposition (EBCVD). In EBCVD, high-energy electrons bombard a substrate covered with adsorbed gaseous precursor molecules. Upon bombardment, the high-energy electrons generate secondary electrons in the energy range of 0–50 eV, and it is these low-energy secondary electrons which likely induce dissociation of the gaseous and adsorbed precursors, and ultimately the formation of nanoscale deposits [11]. The objective of the research described herein is to: i) investigate the viability of low-energy EBCVD as a controlled deposition strategy, and ii) investigate the fundamental chemistry and physics that result from electron-stimulated reactions upon adsorbate-covered single crystal substrates.

1.1 Low-Energy Electron Collisions with Surfaces

1.1.1 Inelastic Scattering of Low-Energy Electrons

When low-energy electrons collide with a molecular target, which includes surfaces, particularly a single crystal covered with adsorbates, a variety of reaction pathways are possible. The primary channels involve elastic and inelastic scattering processes. In this work, we concentrate on the energy loss channels driven by inelastic scattering. For example, upon bombardment, inelastic electron scattering occurs, which induces

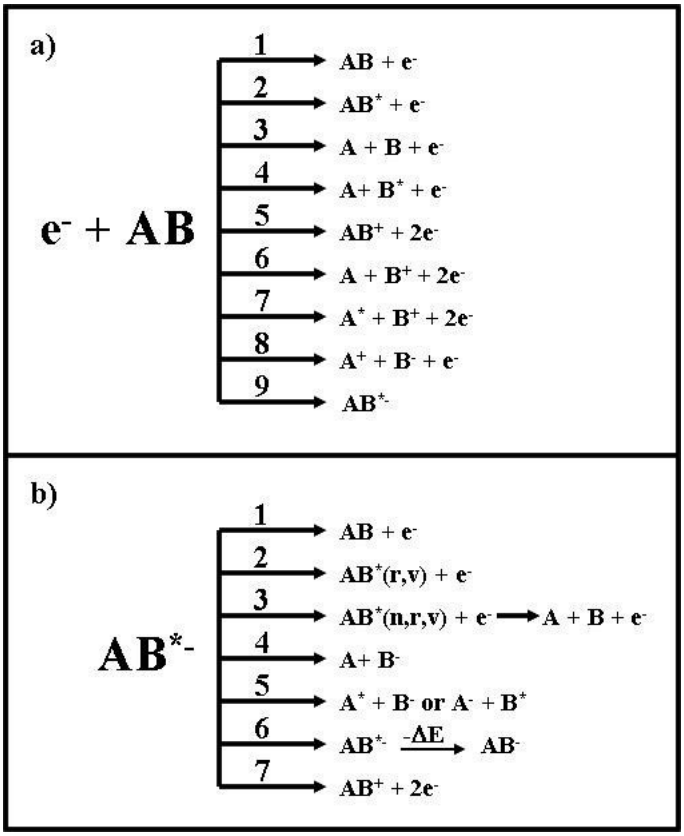

Figure 1.1: a) Possible pathways produced from an electron collision with target molecule AB. b) Dissociation and energy dissipation pathways of the transient negative ion (TNI) created via electron attachment to AB [13].

decomposition of the adsorbates into reactive fragment species. These reactive fragments may then: i) desorb from the surface, ii) react with other molecules adsorbed on the surface, or iii) react with the substrate. A diagram illustrating the various interactions resulting from the collision of an electron in this energy range with a molecule, AB, is presented in Figure 1.1(a) [13]. Possible pathways include: 1) elastic scattering, 2) inelastic scattering, 3) dissociation into neutrals, 4) dissociation into ground and excited state neutrals, 5) ionization of the parent molecule, 6) dissociation into a neutral and a cation, 7) dissociation into an excited state neutral and a cation, 8) ion-pair formation, and 9) electron attachment forming a transient negative ion (TNI).

1.1.2 Dissociative Electron Attachment

Low-energy electrons are very reactive species. Electrons with kinetic energies below the ionization threshold (between 0 and 15 eV) are particularly susceptible to capture by molecules [14]. When an impinging electron is captured by a molecule, an electronically or vibrationally excited molecular anion is formed. This excited molecular anion, also called a transient negative ion (TNI), can subsequently dissociate into energetically stable neutral and anionic fragments. This process is known as dissociative electron attachment (DEA). Figure 1.1(b) presents the possible decay pathways initiated by the formation of a TNI and include: 1) detachment without energy transfer, 2) detachment resulting in a neutral molecule in a rotationally and vibrationally excited state, 3) detachment resulting in a neutral molecule in an electronically, rotationally and vibrationally excited state, 4) dissociation producing a neutral and an ion, 5) dissociation producing an excited state neutral and an anion, 6) energy transfer resulting in the stabilization of the TNI, and 7) ionization through electron emission [15–17].

Transient negative ions can be formed resonantly when an incoming electron is captured by the ground or excited electronic states of the target molecules. Generally, there are two ways by which a TNI can be formed. The simplest TNI is formed when an incident electron is trapped by the centrifugal potential formed from the interaction between the incident electron and the neutral molecule in its ground electronic state. This is referred to as a single particle shape resonance [13, 18]. Shape resonances typically lie at energies above the potential energy surfaces of the neutral molecule ground states. Shape resonances usually decay via autodetachment of the electron, leaving the neutral molecule vibrationally and rotationally excited or via DEA resulting in the formation of anionic and neutral fragments. Shape resonances may also involve electronic excitations. When the energy of the incident electron is large enough to induce excitation of an electron in the neutral molecule, a resonance

can form in which two electrons can occupy a normally unoccupied molecular orbital(s). These resonances are referred to as core excited shape resonances, and like single particle shape resonances, typically decay via autodetachment of the electron or DEA.

Similar to the core excited shape resonance, a Feshbach resonance also involves the excitation of an electron in a neutral molecule. In a Feshbach resonance, the TNI lies below the electronically excited state of the neutral molecule, and therefore cannot relax to that state by ejection of the electron. Consequently, this TNI can only relax to a lower lying excited state or the ground state of the molecule, which requires a rearrangement of the electronic structure through a two electron transition, resulting in the extension of the lifetime of the resonance [13, 14, 17, 18].

1.2 Electron-Stimulated Desorption

The study of surfaces, particularly atoms and molecules adsorbed on surfaces, is relevant in various scientific disciplines. Several spectroscopic and microscopic techniques have been developed to study the chemistry and physics involved with adsorbate-substrate interactions. One of the most versatile and surface-sensitive techniques is electron-stimulated desorption (ESD). The versatility of ESD is evident by the wide range of surface systems that can be probed and the variety of information that can be obtained from studying the interactions of electrons with these surfaces [19]. ESD has been used to study the properties of metals, semiconductors, oxides and alkali-halide solids, as well as the chemistry and physics of adsorbates such as physisorbed noble gases, small chemisorbed molecules and large organic molecules. A wealth of information can be obtained from ESD including the bonding geometry of adsorbed surface species, the thermodynamics of adsorbed species, and the nature of intermolecular forces.

Electron-stimulated desorption involves the removal of ionic and neutral species

from a surface due to low-energy (< 500 eV) electron collisions. The mechanism by which desorption occurs is non-thermal and is not mediated by momentum transfer. Rather, in the case of ESD, desorption is induced by electronic transitions. Several mechanisms have been brought forth to describe electron-stimulated desorption. Perhaps the most well-known description is the Menzel-Gomer-Redhead or MGR model illustrated schematically in Figure 1.2 [20–22].

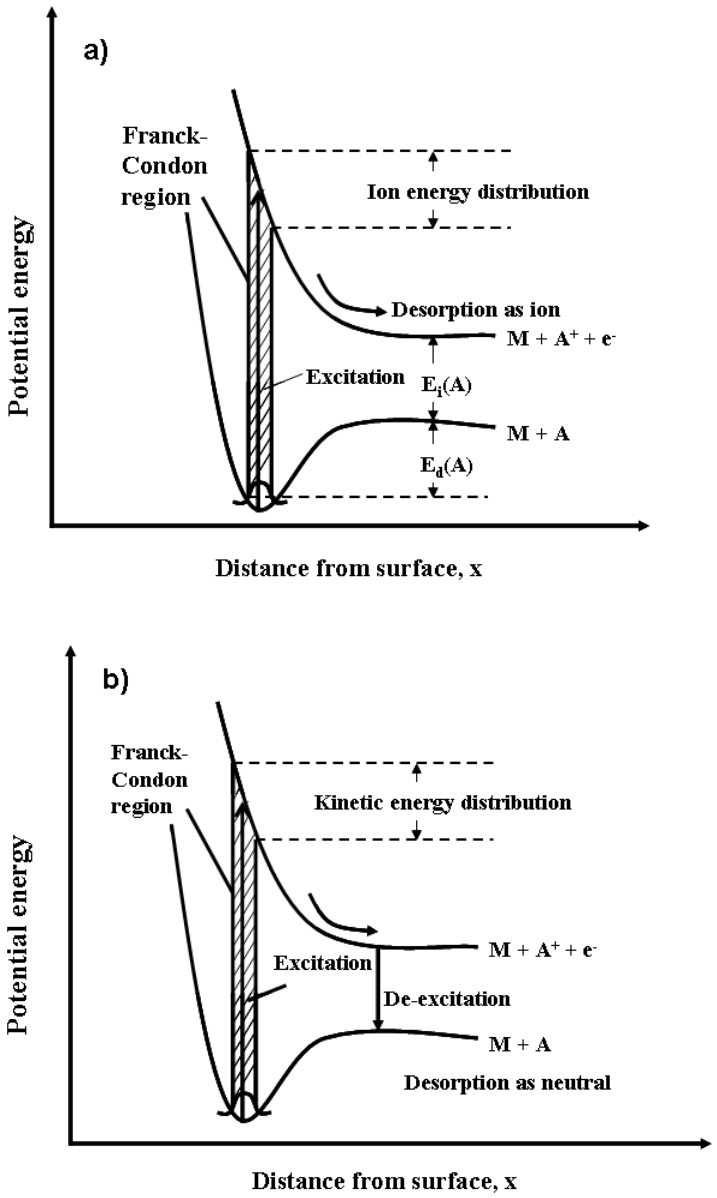

Figure 1.2: Schematic potential energy curves for the interaction between a surface, M and an atom, A. Panel a) illustrates desorption of an ion, A^+ and b) depicts neutral desorption. $E_d(A)$ is the binding energy of the atom to the surface, and $E_i(A)$ is the ionization potential of the atom [20–22].

In the MGR model, desorption is initiated by the excitation or ionization of the adsorbed atom or molecule by electron impact from a ground excited state of the M–A system by a Franck-Condon transition to some excited state. Following excitation, the excited species will relax by moving away from the surface, thus converting potential energy to translational kinetic energy. Barring other interactions, the ion or excited neutral will escape from the surface, appearing in the gas phase with a kinetic energy range as shown in Figure 1.2(a). Desorption of ground state neutral species is also possible, as illustrated in Figure 1.2(b). As with ions, desorption is initiated by excitation from electron impact from the ground electronic state to an excited state. There is a finite probability of the ionic species being neutralized by an electron from the surface, by either Auger processes or resonant tunneling into the empty electronic level of the excited species. Consequently, the excited species is returned to the ground state potential energy curve, but with some kinetic energy. If the neutral species has sufficient kinetic energy, the atom or molecule can escape from the surface.

1.3 Electron Beam Chemical Vapor Deposition

Thus far, Chapter 1 has discussed processes involved in the removal of matter from a surface induced by electron collisions. However, electron interactions with surfaces may also result in deposition of matter on a surface. One technique which utilizes electrons as a mechanism for adsorption of atoms and molecules on a surface is electron beam chemical vapor deposition.

Electron beam chemical vapor deposition, or EBCVD, is the process by which gaseous molecules are decomposed by a beam of electrons, thus leading to the adsorption of non-volatile fragments onto a substrate. The first observations of electron-beam-induced deposition were reported in the 1950s describing the unwanted artifacts formed in electron microscopy due to carbon contamination [23]. An alternative name for this process is electron beam-induced deposition or EBID, which typically implies

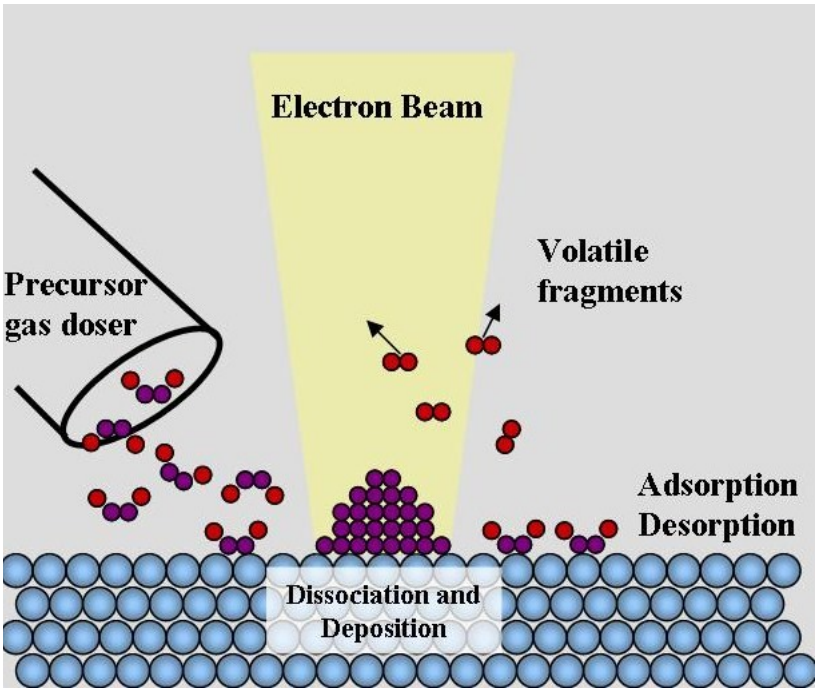

Figure 1.3: Schematic illustrating the electron-beam-induced deposition (EBID) process.

the use of a focused beam of electrons in the energy range of 20–100 keV, and systems are usually modified scanning electron microscopes or transmission electron microscopes, allowing for the introduction of a precursor gas. The EBCVD process is shown schematically in Figure 1.3. First, a precursor gas is introduced to the substrate where the molecules then adsorb, diffuse and desorb at the surface. Following, and in some instances, during exposure to the precursor, the substrate is bombarded with electrons, subsequently inducing dissociation of the precursor molecules resulting in the formation of a solid deposit and volatile by-products which are pumped away [8, 10, 11, 24]. Although the incident electron energy range is 20–100 keV, it is likely the secondary electrons (0–50 eV), generated by the interaction of the high-energy electrons with the surface, that are responsible for inducing dissociation and adsorption [11].

While the initial studies of EBCVD focused on deposition of carbon structures,

there are a variety of precursor molecules that are suitable for forming metallic and ceramic deposits [10]. It should also be noted that, depending on the reagent gas, electron bombardment may result in etching of the surface rather than deposition. Precursors such as hydrochloric acid and silicon tetrachloride are examples of etchants for silicon substrates [13].

1.4 Overview

Chapter 2 describes the deposition of carbon films on a Si(111) substrate via electron-beam chemical vapor deposition (EBCVD). As the device industry continues to push the limits of silicon-based technologies, it is becoming increasingly important to develop alternative materials for integrated circuits. The demand for alternative materials has promoted the synthesis and characterization of a variety of semiconductor materials. One of the most promising semiconductor materials, due to its attractive electronic properties, is silicon carbide. In an effort to grow silicon carbide at relatively low temperatures, a technique referred to as EBCVD was developed. Utilizing acetylene as a precursor molecule, carbon structures were deposited on a single crystal silicon substrate. The films were analyzed by Auger electron spectroscopy and scanning tunneling microscopy and the effects of post-EBCVD annealing are discussed.

Chapters 3, 4, and 5 discuss the experiments investigating the fundamental chemistry and physics that govern the EBCVD growth of carbon films on silicon from an acetylene precursor. Chapter 3 provides a detailed description of the C_2H_2-Si(111) adsorbate-substrate system, focusing primarily on the bonding geometry and the electronic structure. Chapters 4 and 5 discuss work that involves the electron-stimulated reactions within the C_2H_2-Si(111) system. Specifically, Chapter 4 describes the electron-stimulated desorption of cations from acetylene adsorbed on silicon, while

Chapter 5 focuses on the production and release of neutral desorbates from the surface.

The remaining chapters detail work involving the study of graphene oxide and graphene. These materials are examples of other alternative materials, in addition to silicon carbide, that are being developed as replacements for silicon. Chapter 6 continues along the lines of Chapter 4, outlining the experimental work conducted on low-energy electron collisions with graphene films epitaxially grown on 65-SiC(0001). Chapter 7 discusses the interaction of low-energy electrons with graphene oxide. Similarly to Chapters 4 and 6, the electron-stimulated desorption of cations is described. Additionally, the viability of low-energy electrons as a method for reducing graphene oxide to graphene is discussed.[1]

[1]The chapters describing the ESD of acetylene adsorbed on Si(111)-(7×7) as well as Chapters 6 and 7 are manuscripts in preparation for publication in peer-reviewed journals.

CHAPTER II

ELECTRON BEAM CHEMICAL VAPOR DEPOSITION OF CARBON ON SILICON(111) FROM AN ACETYLENE PRECURSOR

2.1 Introduction

Silicon carbide (SiC) is a wide bandgap semiconductor that has attracted much interest due to its favorable thermal, chemical and mechanical properties. However, despite these intriguing properties, SiC has yet to emerge as a major material used in electrical and optoelectronic devices because of the difficulty in producing high-quality, defect-free SiC wafers.

The typical method for growing semiconductor crystals involves melting and recrystallizing semiconductor material into large crystals with the aid of a seed crystal. This technique is known as the Czochralski process [25] and is commonly used for growing silicon, germanium, and gallium arsenide wafers. However, SiC cannot be grown via the Czochralski method because SiC sublimes, rather than melts, at reasonable temperatures and pressures. An alternative method for forming SiC crystals is the Lely process [26]. In the Lely process, polycrystalline powdered SiC is sublimed and the condensed on the walls of the reaction vessel, forming small, hexagonal platelets. Although the Lely process does not require a seed crystal like with the Czochralski method, the SiC crystals formed are small and the size distribution is not reproducible. In the late 1970s, the modified Lely method was developed [27, 28]. In the modified Lely method, polycrystalline SiC is heated to sublimation and the SiC vapor is condensed on a SiC seed crystal, forming cylindrical, crystalline SiC ingots which are then cut into wafers. From the development of the modified Lely

method, reproducible single crystals of SiC are commercially available.

Although SiC single crystal wafers are now commercially available, the growth of SiC on silicon single crystals is desirable. The capability to produce SiC on large area silicon substrates would provide inexpensive wafers which are compatible with current silicon-based technologies. The prominent method by which SiC is grown on silicon is chemical vapor deposition (CVD) [30]. The chemical vapor deposition growth of SiC involves heating a Si(100) or Si(111) substrate to an elevated temperature (ranging from 600 °C to 1400 °C) whilst exposing the surface to a carbonaceous precursor gas. Unlike the Czochralski and physical vapor transport methods, which result in the formation of hexagonal 4H- or 6H-SiC, chemical vapor deposition growth of SiC on silicon yields cubic 3C-SiC only. The major challenge for forming crystalline SiC on silicon is the large lattice mismatch of 20% between SiC and Si [3, 30–33]. This large mismatch in the lattice constants gives rise to a high density of crystallographic defects in the 3C-SiC layers. There are a variety of defects that can be present in SiC including: screw dislocations, micropipes and stacking faults [4]. Screw dislocations occur when strain causes successive dislocations within the atomic plane of a crystal lattice, forming a spiral shape or helix. When screw dislocations propagate through the crystal, extended, hollow, tube-shaped defects called micropipes are formed. Although strain plays an important role in the formation of defects in SiC crystals, the high temperatures required for processing SiC in conventional CVD growth also contributes to defect formation [34]. High processing temperatures also result in the sublimation of Si atoms from the SiC lattice, resulting in the formation of SiC alloys instead of a 1:1 stoichiometric ratio of Si to C. Therefore, it would be advantageous to utilize a low-temperature growth method to produce crystalline SiC films on Si substrates. In this chapter, the development and implementation of a low-temperature growth method called electron-beam chemical vapor deposition

(EBCVD) is discussed. EBCVD was used to deposit thin carbon films from an acetylene precursor on a Si(111) single crystal. The resulting films were characterized via scanning electron microscopy (SEM) and Auger electron spectroscopy (AES).

Auger electron spectroscopy is a powerful tool for the analysis of the chemical composition of surfaces. The basis of this technique is the Auger effect which describes the ejection of electrons from an excited atom after a succession of relaxation events. An Auger process involves the excitation of an atom due to a collision with an incident electron with kinetic energy of 3 keV to tens of kilovolts. This collision event results in the removal of a core electron. To regain stability, an electron from a shallower level will fill the core hole. The energy loss associated with the relaxation of the valence level electron is equal to the difference of the orbital energies of the core electron and the valence electron. A second electron from the valence level may be ejected from the atom if the transition energy difference is greater than the orbital binding energy. This second ejected electron is referred to as the Auger electron. Since orbital energies are specific for each element, analysis of the Auger electron can provide information regarding the chemical makeup of a surface. The kinetic energy of the Auger electron is can be calculated as shown in Equation 1, where E_{Auger} is the kinetic energy of Auger electron, E_K is the binding energy of the core level, and E_{L1} and E_{L2} are the binding energies of the valence levels. A schematic of the Auger process is presented in Figure 2.1.

$$E_{Auger} = E_K - E_{L1} - E_{L2} \tag{1}$$

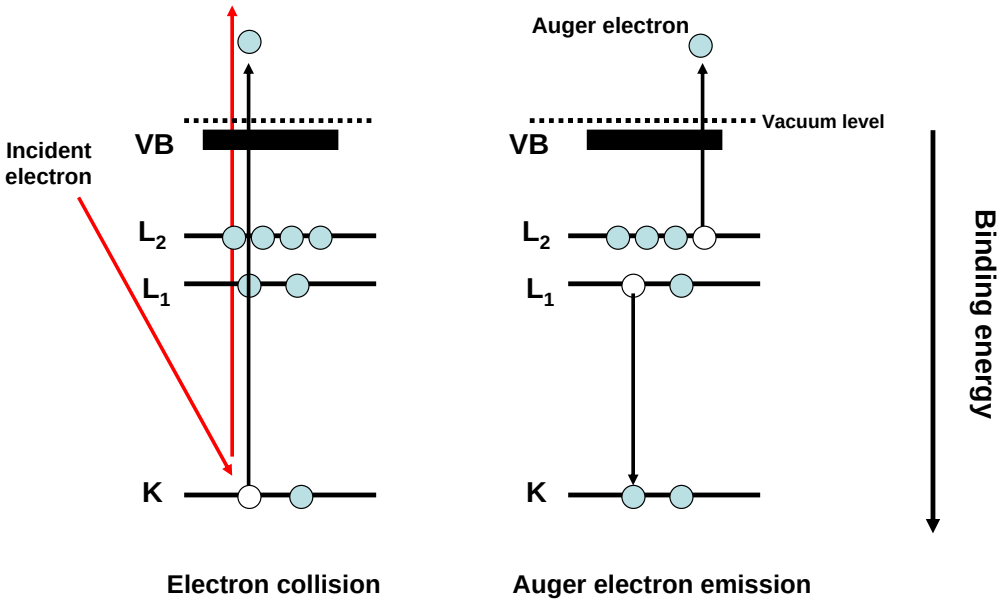

Figure 2.1: Schematic illustrating the Auger process.

2.2 Experimental Details

The EBCVD experiments were carried out in a custom-built ultrahigh vacuum (UHV) chamber with a base pressure of 5×10^{-10} torr. The chamber is equipped with a quadrupole mass spectrometer (QMS), a pulsed, tunable (5–1000 eV) electron gun, a variable leak valve coupled to a differentially pumped dosing manifold, and a differentially pumped load-lock system.

The substrate is the (111) face of an n-type silicon single crystal which is spot welded to a molybdenum sample holder disk. The silicon sample was cleaned by repeatedly annealing to 1100 °C via electron bombardment. Carbon was deposited on the silicon substrate, which was heated to 650 °C, by exposing the surface to 1800 L of acetylene (1 Langmuir (L) = 1×10^{-6} torr $\cdot$ s). Following exposure to acetylene, half of the surface was irradiated with 8 eV electrons for 20 minutes. The resulting film was

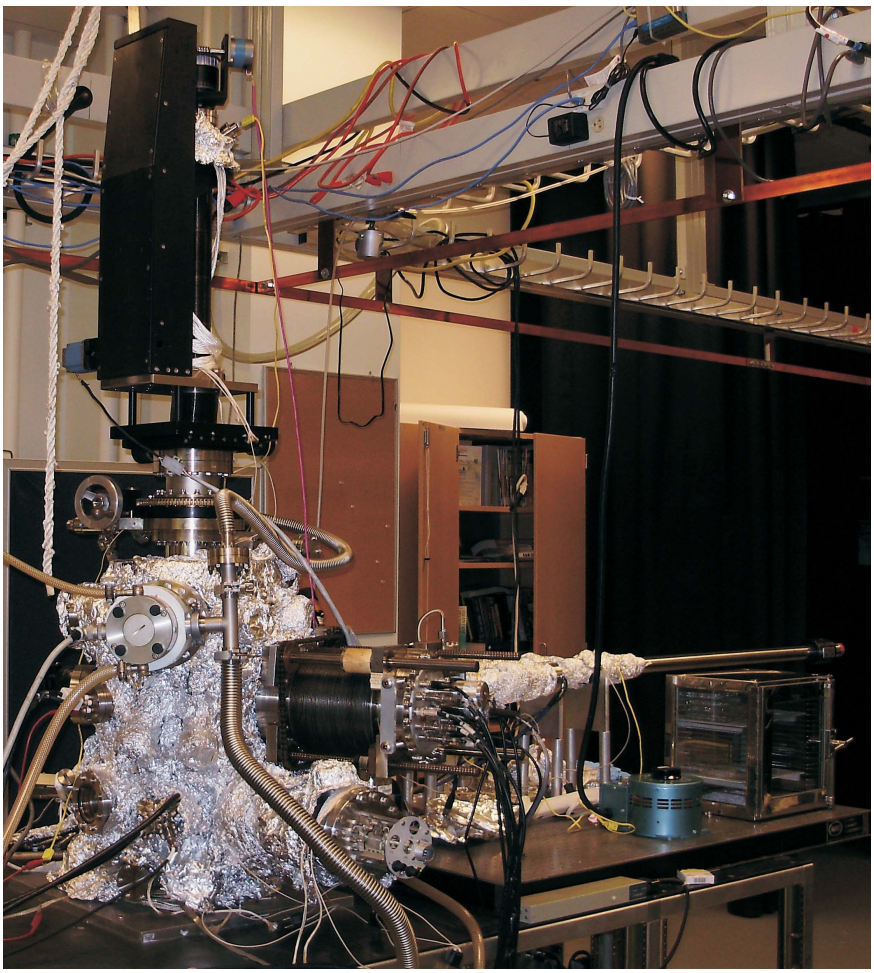

Figure 2.2: The custom-built EBCVD ultrahigh vacuum chamber.

characterized by scanning electron microscopy (SEM), Auger electron spectroscopy (AES) and low energy electron diffraction (LEED).

2.3 Results

2.3.1 Scanning Electron Microscopy Images

Scanning electron microscopy images were obtained for carbon films deposited on silicon from both conventional chemical vapor deposition and electron beam chemical vapor deposition and are shown in Fig 2.3.

The resulting carbon deposits differ considerably in topography. The deposit grown from conventional CVD is film-like with pores distributed across the surface.

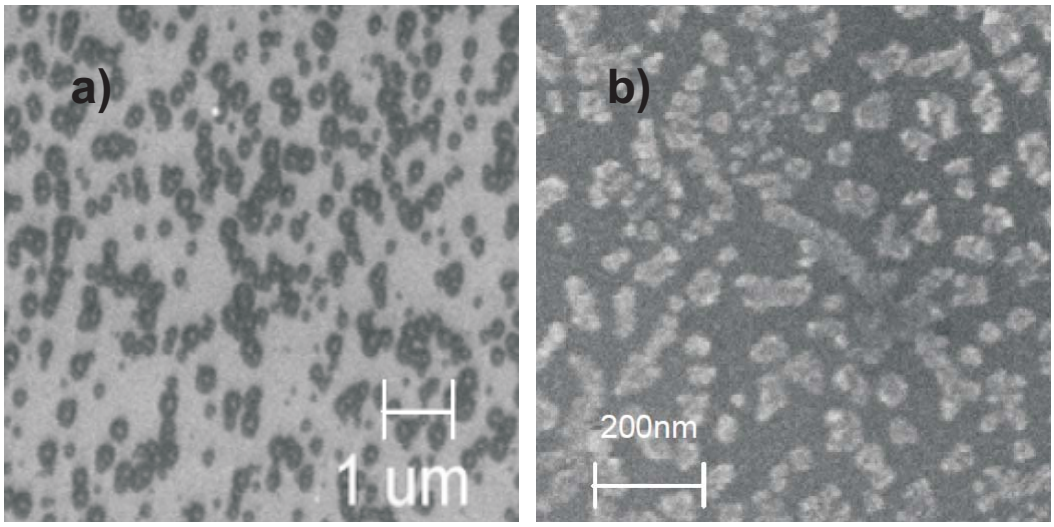

Figure 2.3: SEM images of carbon films deposited on Si(111) via a) conventional CVD and b) EBCVD.

The pores, which extend to the underlying silicon surface, range in diameter from 50–500 nm. EBCVD of acetylene on silicon results in the formation of carbon nanoparticles which range in size from 50–200 nm. Though the carbon nanoparticles resulting from EBCVD vary in shape and size, they are evenly distributed across the silicon substrate.

2.3.2 Auger Electron Spectra

In order to obtain information regarding the chemical nature of films grown via CVD and EBCVD, Auger electron spectra were obtained for both surfaces. Figure 2.4 presents the Auger electron spectra of both the surface resulting from CVD (blue curve) and EBCVD (red curve). The primary features in the spectrum are the silicon KLL peaks at 80 eV and 90 eV, the carbon KLL peak at 268 eV and 272 eV, and the oxygen KVV peak at 500 eV. The Si LVV region of both the CVD and EBCVD surfaces is a doublet, which is indicative of oxidation [35, 36]. This oxidation is confirmed by the presence of the O (KVV) peak at 500 eV. It is likely that oxidation of the surface occurred during transfer of the sample to the AES chamber, during

which the sample was exposed to atmosphere.

Particular attention is given to the shape, position and intensity of the carbon KLL region. Although there are negligible differences in shape and intensity of the large minima of the CVD and EBCVD samples, there is a considerable shift in energy. The CVD minimum is located at 267 eV, whereas the EBCVD minimum is shifted higher in energy to 272 eV.

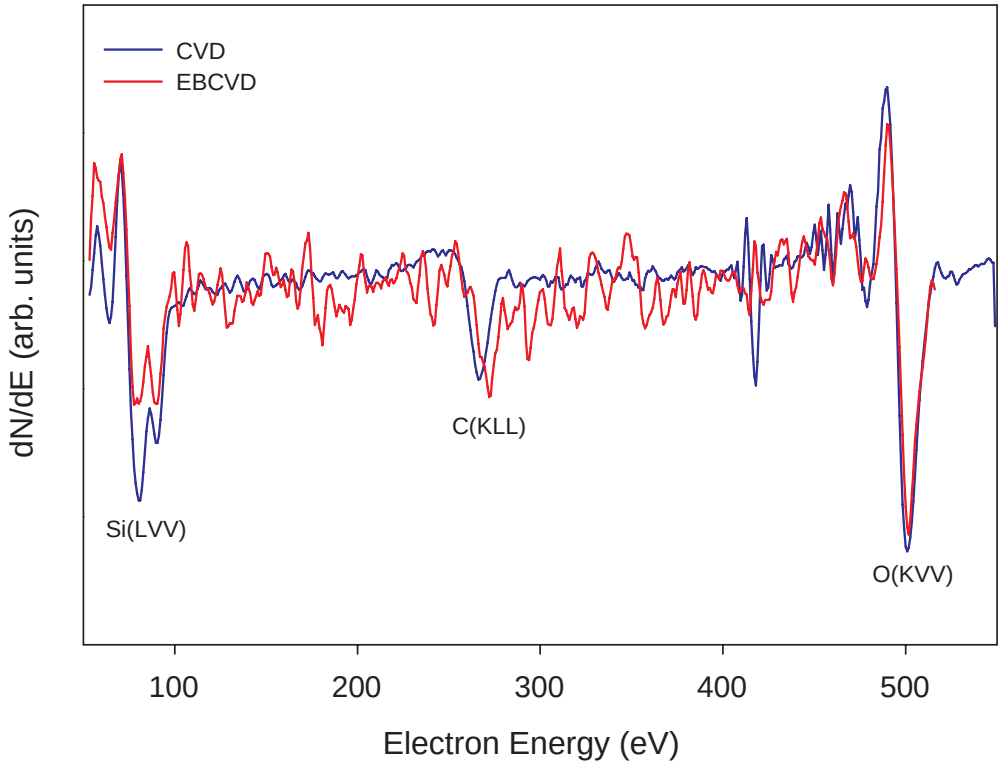

Figure 2.4: Auger electron spectra of the Si(111) surface following CVD (blue curve) and EBCVD (red curve) using an acetylene precursor.

2.4 Discussion

2.4.1 Analysis of Carbon KLL Auger Spectra

In addition to the obvious physical, topographical differences of the non-irradiated CVD surface and the irradiated EBVCD surface, information regarding the dissimilarity in the chemical nature of the two deposits was investigated with Auger electron spectroscopy. A wealth of information regarding the bonding of carbon can be obtained by analysis of the shape of the peaks that make up the C KLL region of the Auger spectrum. The shape of the main minimum, as well as the surrounding satellite peaks of the C KLL region vary depending on the carbon bond hybridization [37–43]. Due to this shape effect, it is possible to distinguish between sp^3, sp^2 and amorphous carbon, as well as silicon carbide.

In the KLL region of the Auger spectrum, silicon carbide, graphite, diamond, and amorphous carbon all feature a main minimum at 273 eV. The amorphous carbon spectra also contain a shoulder within the main minimum at 280 eV. SiC and graphite can be distinguished from each other by distinct features in the satellite peaks that appear at lower energy. Immediately preceding the main minimum feature in the SiC Auger spectrum is a sharp maximum at 264 eV (first satellite), followed by a small minimum at 257 eV (second satellite). For graphite, the main minimum is preceded by a weak maximum and minimum at 256 eV (first and second satellites), followed by a sharp maximum at 246 eV (third satellite).

Taking into consideration these fingerprint features in the C KLL region, it is possible to draw some conclusions about the chemical nature of the CVD and EBCVD films. The 5 eV shift for the main minimum feature of the CVD carbon KLL spectrum is likely due to charging effects [42]. It is difficult to assign the carbon deposits from CVD and EBCVD as completely sp^2, sp^3 or SiC, however the EBCVD spectrum appears to be graphitic in nature. Similarly to the graphite spectrum described earlier, the EBCVD carbon KLL region is comprised of a main minimum at 272

eV and is preceded by three satellite peaks: a weak maximum at 262 eV, a weak minimum at 258 eV and a sharp maximum at 253 eV.

2.4.2 Effect of Low-Energy Electron Bombardment

As demonstrated from the SEM images and Auger electron spectra reported in this chapter, low-energy electrons can affect the chemical and physical structure of an adsorbate. The objective of the low-energy EBCVD experiments outlined in this chapter is to access dissociative electron attachment resonances in acetylene to induce chemisorption of carbon onto a silicon surface. An additional benefit to this DEA approach is that it is also possible to induce desorption of unwanted species.

There are many DEA resonances for the acetylene molecule, particularly in the electron energy range of 5–10 eV [44]. Gas phase DEA studies [44] show that the predominant products from low-energy electron bombardment with acetylene are C_2H^- and $C_2{}^-$ at incident electron energies of 7.5–8.0 eV. In particular, the $C_2{}^-$ and two H atoms dissociation products correlate with the $^2(3s3p\pi)$ Rydberg state.

Taking this reaction pathway into consideration, an incident electron energy of 8 eV was chosen for the EBCVD experiments. The formation of the $C_2{}^-$ anion and two H atoms at this electron energy may also offer an explanation for the graphitic features in the EBCVD Auger spectrum. At 8 eV, the carbon-carbon bonds remain in tact, and do not break further yielding C^-, which would present sp^3 character in the carbon KLL region of the Auger spectrum. While it is difficult to pinpoint the reason for the dramatic differences in the physical nature of the irradiated and non-irradiated deposits, it is plausible that electron bombardment of the EBCVD film resulted in the desorption of some material, resulting in the particle nature of the EBCVD deposit.

The electron-beam chemical vapor deposition experiments outlined in this chapter demonstrate the viability of low-energy electrons, in conjunction with a conventional

deposition technique, as a low-temperature growth strategy for graphitic carbon layers on a silicon single crystal. Auger electron spectroscopy and scanning electron microscopy confirm that low-energy electrons do alter the chemical and physical structure of carbon deposit. Further investigation of the mechanisms involved in low-energy electron induced processes on the acetylene/Si(111) surface are described in Chapters 4 and 5.

CHAPTER III

ACETYLENE ADSORBED ON THE SILICON(111) SURFACE

3.1 Introduction

The study of the interaction of organic molecules with the silicon surface, particularly adsorption and other surface reactions, are topics of fundamental and technological relevance. Hydrocarbons have been the focus of several studies due to their technological importance in the epitaxial growth of SiC, diamond and graphitic films on the silicon surface [45, 46]. In the case of SiC, acetylene has emerged as an attractive precursor for the epitaxial growth of 3C-SiC and silicon-carbon alloys [34, 47–50].

The Si(111) surface is an interesting substrate, particularly the Si(111)-7×7 reconstructed surface. The complexity of the 7×7 reconstruction results in a number of adsorption sites for the acetylene molecule. A detailed description of the Si(111)-7×7 surface, and the manner in which acetylene adsorbs on it, is necessary in order to understand the results presented in Chapters 2, 4 and 6. In this chapter, a comprehensive overview of the electronic structure and bonding geometry of the Si(111)-(7×7):C_2H_2 system is discussed.

3.2 Bonding Geometry and Saturation Coverage

3.2.1 The Si(111)-(7×7) Surface

The experimental conditions required to clean a Si(111) surface, high temperatures and ultrahigh vacuum pressures, result in the rearrangement of the surface atoms to an energetically stable structure called the 7×7 reconstruction [51]. The 7×7 configuration gives rise to several different atomic positions in the top three layers of

the crystal structure. The structural model describing the Si(111)-(7×7) surface is known as the dimer-adatom-stacking fault or DAS model and is shown schematically in Figure 3.1 [51]. In the DAS model, the Si(111)-(7×7) surface is comprised of three layers stacked on top of the base Si(111)-(1×1) unstructured surface. Immediately above the base layer is the dimer layer, which forms due to the removal of an atom with a dangling bond and one of its nearest neighbors, leaving four atoms with unsatisfied bonds. To regain stability, the atoms of the underlying layer shift, allowing the formation of dimers. Consequently, this shift of the underlying surface atoms gives rise to the formation of faulted and unfaulted zones on the Si(111)-(7×7) surface. Atop the dimer layer lies the rest atom layer, which consists of 3-coordinated Si atoms. The topmost layer is the adatom layer, which has dangling bonds oriented upward into the vacuum. The stable Si(111)-(7×7) reconstructed surface has 19 dangling bonds per unit cell, as opposed to the 49 dangling bonds of the Si(111)-(1×1) surface. The 19 dangling bonds are comprised of 12 adatoms, 6 rest atoms, and 1 corner atom. Further evidence of the complexity of the Si(111)-(7×7) surface is realized by the fact that the 19 dangling bonds are distributed among 7 inequivalent types of Si atoms: the corner hole adatom, the corner and center adatoms on both the faulted and unfaulted halves, and the faulted and unfaulted rest atoms [46].

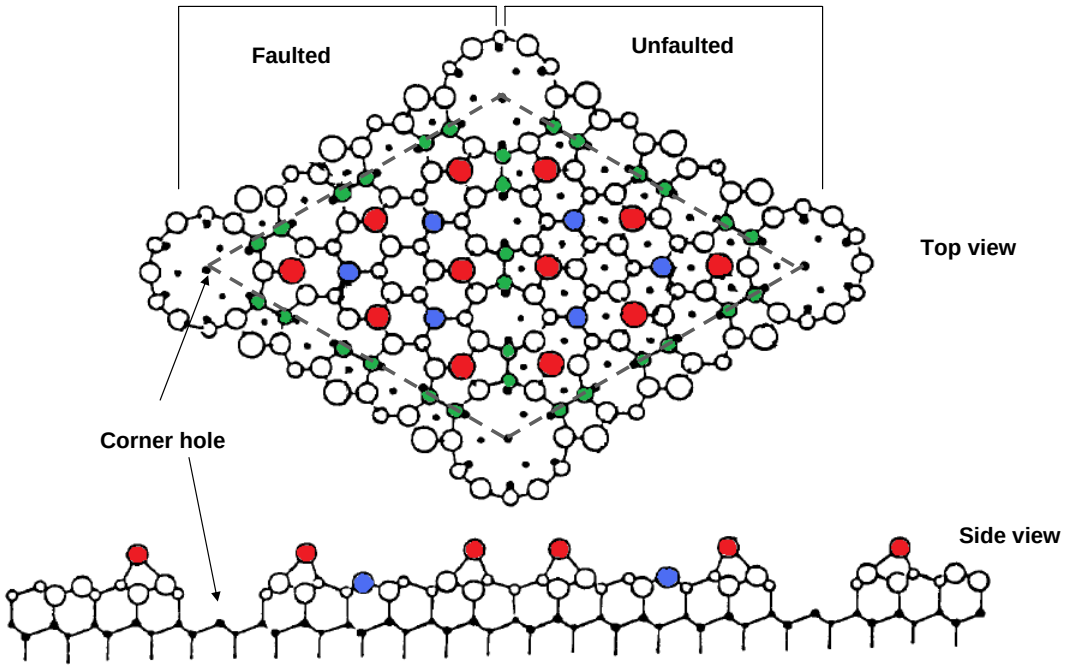

Figure 3.1: The DAS model of the Si(111)-(7×7) surface (adapted from Ref. 51). In the top view, the gray dashed line outlines the unit cell. The different types of silicon atoms are shown in the top and side views. Dimers are represented as green circles, rest atoms are shown as blue circles and adatoms are red circles.

3.2.2 Acetylene Adsorption on the Si(111)-(7×7) Surface

The manner in which acetylene bonds to the Si(111)-(7×7) surface is an important element in understanding the mechanisms governing SiC formation from epitaxial growth. As discussed earlier in this chapter, the Si(111)-(7×7) surface is very reactive due to the 19 dangling bonds protruding from the terminal layer. Investigations reveal that the dangling bonds of adjacent adatom-rest atom pairs behave as di-radicals [52, 53]. The Si_2 di-radical reacts with the acetylene molecule forming two Si–C bonds. This bonding geometry is termed the di-σ bond configuration and was first observed experimentally for this system by Yoshinobu, et al [52, 53]. A schematic of acetylene di-σ bonded to Si(111)-(7×7) is shown in Figure 3.2. In the di-σ bonded configuration, the acetylene triple bond is broken, leaving a C–C double bond, resulting in an ethylene-like bonding geometry.

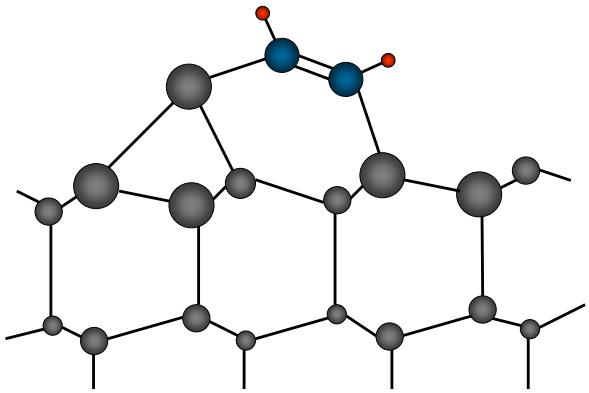

Figure 3.2: Schematic of an acetylene molecule di-σ bonded across two adjacent Si atoms of the Si(111)-(7×7) surface (adapted from Ref. 52 and 53). Silicon atoms are represented as gray spheres, carbon atoms as blue spheres and hydrogen atoms as red spheres.

Although the Si(111)-(7x7) surface has 19 dangling bonds, not all neighboring Si atoms are conducive for acetylene chemisorption. According to the DAS model, there

are seven combinations of two neighboring Si atoms that have dangling bonds. The possible dimer configurations and the bond distances between the two Si atoms are shown in Table 3.1.

Table 3.1: The seven possible Si atom pairs of the Si(111)-(7×7) surface and the corresponding Si–Si distance. Adapted from Ref. 52.

Possible Si–Si Pairs	Si–Si Distance (Å)
Corner Adatom–Corner Adatom	6.65
Corner Adatom–Center Adatom	7.68
Center Adatom–Center Adatom (within a subunit)	7.68
Center Adatom–Center Adatom (across a dimer row)	6.65
Corner Adatom–Corner Hole	7.85
Corner Adatom–Rest Atom	4.57
Center Adatom–Rest Atom	4.56

In order for acetylene to chemisorb, the distance between the Si atom pair cannot exceed 5.7 Å, which corresponds to the bond distances of two Si–C bonds and one C–C bond. This constraint eliminates all possible Si–Si pairs except for the corner adatom-rest atom and center adatom-rest atom configurations. Therefore, it is most likely that acetylene di-σ bonds to corner or center adatom to rest atom pairs. This inference was confirmed by the STM measurements made by Yoshinobu and coworkers [52]. Their STM work also revealed that acetylene preferentially chemisorbs to center adatom-rest atom pairs over corner adatom-rest atom pairs in a 2:1 ratio. This can be attributed to the fact that center adatoms have two neighboring rest atoms, whereas corner adatoms have only one.

Additionally, acetylene molecules preferentially adsorb to the atoms in the faulted zones of the Si(111)-(7×7) unit cell rather than the unfaulted zones. This may be due to the differences in the strain energy of the faulted and unfaulted regions. Another possibility may be the difference in the electronic structure of the faulted and unfaulted zones, more specifically, the proximity of the density of states to the Fermi level [54].

The aforementioned factors contributing to the preferential bonding geometry of acetylene to Si(111)-(7×7) offer insight in the determination of the saturation coverage. Acetylene chemisorbs on the Si(111)-(7×7) surface even at relatively low temperatures (100–120 K) [55]. Physisorption of acetylene on this surface requires even lower temperatures (40–50 K) [56]. Thus, the saturation coverage of acetylene on Si(111)-(7×7) at room temperature (298 K) is 0.245 ML [57].

3.3 Electronic Structure

In order to understand the results presented in the next few chapters, a comprehensive description of the electronic structure of acetylene and acetylene adsorbed on silicon is required. The ground state electronic configuration of acetylene is $(1\sigma_g)^2$ $(1\sigma_u)^2$ $(2\sigma_g)^2$ $(2\sigma_u)^2$ $(3\sigma_g)^2$ $(1\pi_u)^4$. Photoelectron spectroscopy of gaseous [58] and condensed [59] acetylene show that the occupied molecular orbitals of gas phase and solid acetylene are clearly visible, and although the spectrum for solid acetylene is broadened, the molecular orbitals correspond with those of the gas phase. The energies of the occupied molecular orbitals as determined by photoelectron spectroscopy are shown in Table 3.2. The shift in the ionization potential of condensed acetylene is likely due to screening of the hole in the solid [60].

Table 3.2: Ionization potentials of the occupied molecular orbitals of gaseous and condensed acetylene [58, 59].

	Ionization Potentials (eV)	
Orbital	C_2H_2(g)	C_2H_2(s)
$1\pi_u$	11.43	11.04
$3\sigma_g$	16.76	16.24
$2\sigma_u$	18.71	17.99
$2\sigma_g$	23.65	22.83

Although a great deal of information can be gathered from analysis of the electronic structures of free acetylene and the acetylene molecular solid, it is necessary to

consider the electronic structure of the entire Si(111)-(7×7):C_2H_2 adsorbate/substrate system. The electronic structure of this system has been studied by x-ray photoemission spectroscopy (XPS) and near-edge x-ray absorption fine structure spectroscopy (NEXAFS) [57, 61], and ultraviolet photoemission spectroscopy (UPS), as well as high-resolution electron-energy-loss spectroscopy (HREELS) [50]. As revealed in Yoshinobu's model, two surface states of the silicon surface are involved in the chemisorption of acetylene: the adatom surface state and the rest atom surface state. These surface states overlap with the π and π^* states of the acetylene molecule. The manner in which the adatom and rest atom states overlap with those of the acetylene molecule is depicted schematically in Figure 3.3 [50]. The adatom surface state is partially filled and overlaps with the empty π^* state of acetylene, forming a partially filled bonding state (π^*–AD) and an empty antibonding state (π^*–AD)* above the Fermi level. The rest atom state, which is filled, overlaps with the acetylene π state, which gives rise to bonding (π–R) and antibonding (π–R)* states. Both the rest atom state and acetylene π orbital are filled, therefore the antibonding and bonding states that result from their overlap are also filled. Consequently, the electrons in the filled (π–R)* are donated into the partially filled (π^*–AD) bonding state.

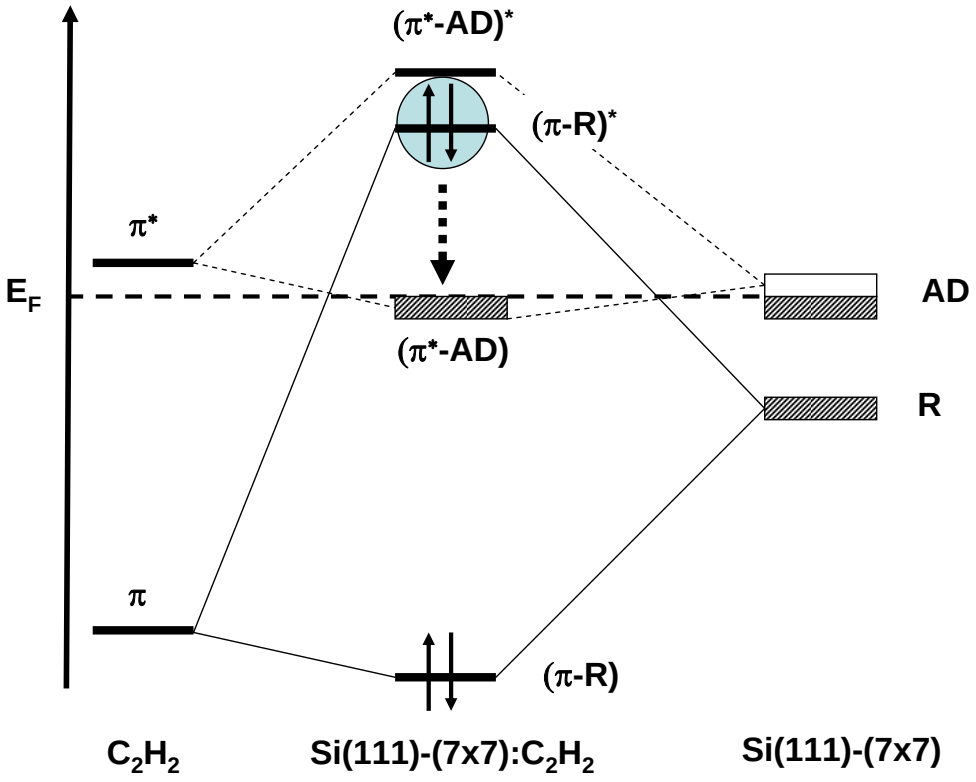

Figure 3.3: Electronic structure diagram of acetylene di-σ bonded to the Si(111)-(7×7) surface [50, 57, 61]. The antibonding electrons of the (π–R)* state (enclosed in the blue circle) are donated into the (π–AD)* state, as indicated by the dashed arrow, giving the Si(111)-(7×7):C_2H_2 system bonding character.

The XPS, NEXAFS, HREELS and UPS investigations described earlier provide a qualitative picture for the electronic structure of acetylene adsorbed on Si(111)-(7×7) by illustrating the bonding and antibonding states formed from the overlap of the and π and π^* orbitals of acetylene and the surface bands of silicon. Figure 3.4 is a schematic energy level diagram, with corresponding energy values, compiled from photoemission spectra of solid acetylene and clean Si(111)-(7x7) [60, 62]. On the left side of the diagram is the density of states of the Si(111)-7x7 surface. The A_3 surface state is labeled and has an energy of approximately 12 eV [62]. The occupied molecular orbitals of acetylene are illustrated on the right with descriptions of the atomic orbitals involved at given energies.

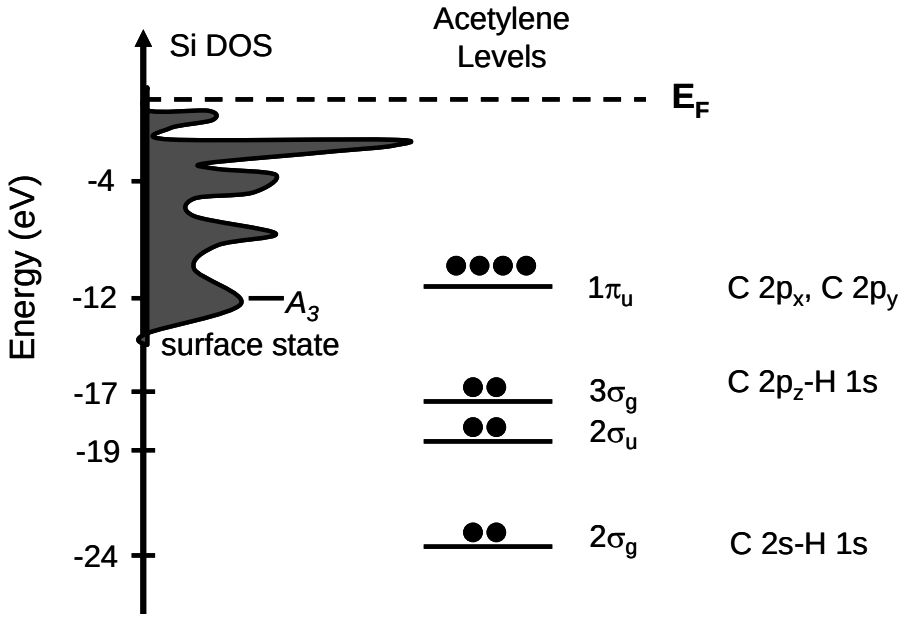

Figure 3.4: Schematic of the energy level diagram of clean Si(111)-(7×7) and acetylene referenced to the Fermi level. The values on the left are compiled from UPS data from Fock, et al. [59] and Rowe, et al. [62]. The Si(111)-(7×7) UPS data was traced from Rowe, et al. [62].

CHAPTER IV

ELECTRON-STIMULATED DESORPTION OF CATIONS FROM DEUTERATED ACETYLENE ADSORBED ON THE SILICON(111) SURFACE

4.1 Introduction

While there have been several studies investigating the interaction of electrons with acetylene in the gas phase [63–73], few studies have been conducted on the interaction of electrons with condensed [56, 74] acetylene. Further, there have been no measurements examining the low-energy electron-induced desorption of cations and neutrals from acetylene adsorbed on Si(111). In this chapter, a detailed examination of the electron-stimulated desorption (ESD) of cations from acetylene adsorbed on Si(111)-(7×7) is presented. Focusing primarily on the threshold energies of the desorbates, mechanisms leading to desorption are proposed.

4.2 Experimental Details

The experiments were performed in a custom designed ultrahigh vacuum (UHV) system with a base pressure of 5×10^{-10} torr which is depicted schematically in Figure 4.1. The substrate is the (111) face of an *n*-type silicon single crystal substrate mounted to a rotatable liquid nitrogen cooled cryomount. The temperature of the sample can be varied from 120 to 1320 K via resistive heating. A type-K thermocouple, shrouded in tantalum foil and clipped to the substrate is used to monitor the temperature. The chamber is equipped with a quadrupole mass spectrometer (QMS), a tunable (5 to 1000 eV), pulsed electron gun oriented 45° relative to the silicon substrate, and a time of flight mass spectrometer (TOF-MS). The TOF-MS is mounted directly below

the substrate where the desorbing cations are detected.

Prior to dosing, the silicon crystal was cleaned by repeatedly annealing the substrate to 1300 K. After cooling to 120 K, the sample was exposed to 3000 L of C_2D_2 (Cambridge Isotope, 99% pure), which leads to the saturation coverage of acetylene on Si(111) [61]. Deuterated acetylene was used to distinguish the hydrogen desorbed from the acetylene on the surface from the background hydrogen in the chamber.

ESD threshold measurements were obtained by scanning the incident electron energy in 1 eV increments from 5 to 50 eV. An electron beam pulse width of 1 μs was used, which effectively integrates over the entire kinetic energy distribution. To maximize collection efficiency, the sample was grounded and a -255 V, 100 μs extraction pulse to the time-of-flight mass spectrometer entrance grid immediately following every electron pulse. Cations generated from the electron bombardment of the surface were extracted by the negative potential pulse. The short electron pulses of 1 μs were used to minimize charging of the substrate and a frequency of 500 Hz allowed for complete discharge between pulses. All data points correspond to the integrated area below each specific mass peak.

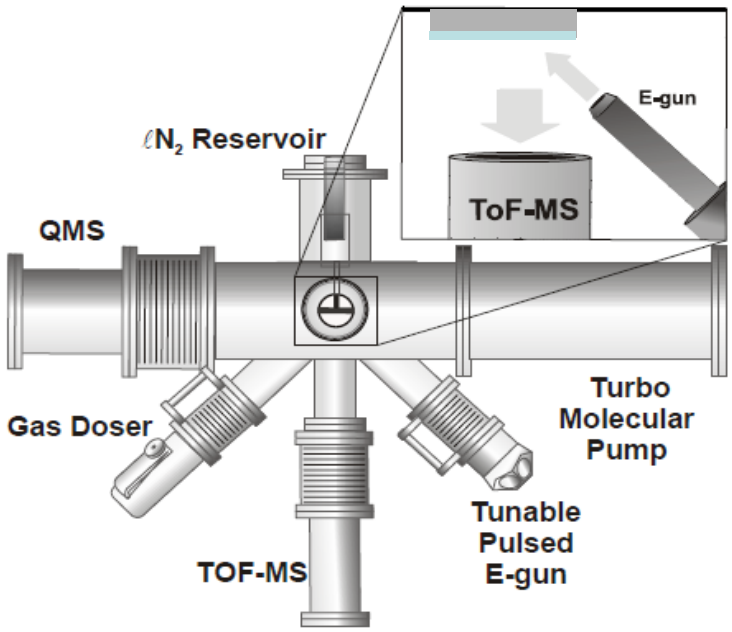

Figure 4.1: Illustration of the UHV chamber where the ESD experiments were performed.

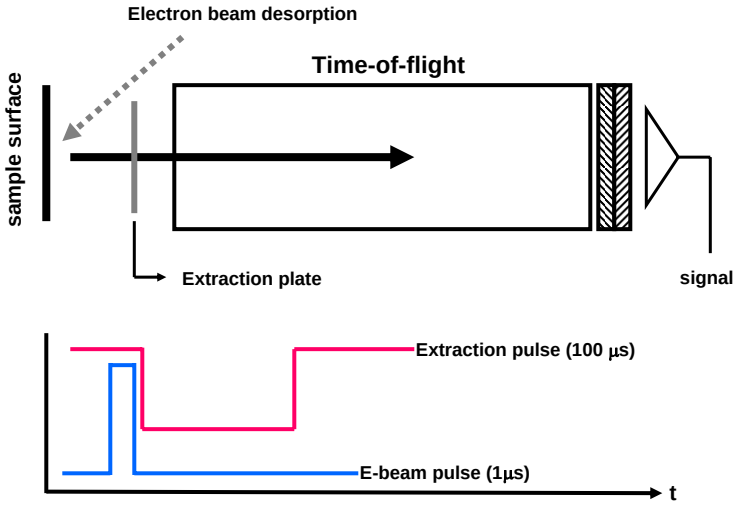

Figure 4.2: Diagram of the ESD-TOF-MS experiment with the pulse sequence used for detection of the cations.

4.3 Results

4.3.1 Threshold Data

The ESD-TOF mass spectrum of acetylene adsorbed on Si(111)-(7×7) is presented in Figure 4.3. The primary cationic desorption products observed were D^+ and $C_2D_2{}^+$ with a small amount of CD^+ and C_2D^+ and C_2HD^+. However, it is important to note that the CD^+ yield was negligible and therefore not included in the yield versus incident electron energy spectra. Other prominent peaks are H^+ and H_3O^+ which can be attributed to background water in the chamber.

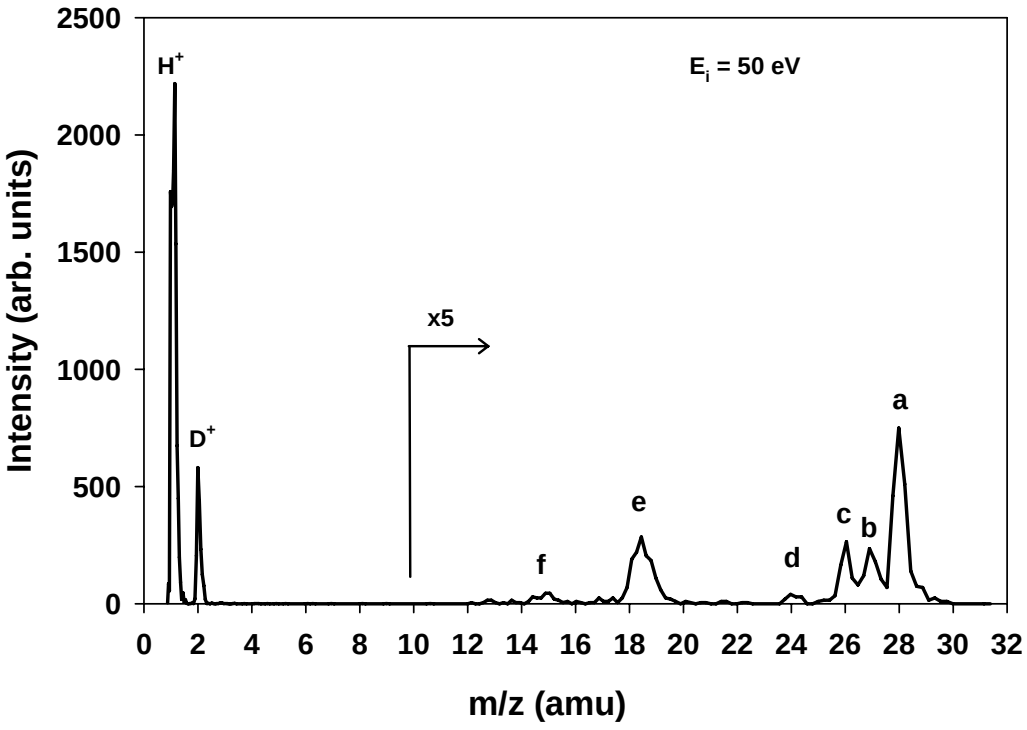

Figure 4.3: Typical TOF-MS of cations emitted from ESD of C_2D_2 adsorbed on Si(111)-(7×7) at 50 eV. The high mass fragments are multiplied by a factor of 5 for ease of comparison. The assignments for the peaks labeled a–f are: a) $C_2D_2{}^+$, b) C_2HD^+, c) C_2D^+ (or possibly $C_2H_2{}^+$), d) $C_2{}^+$, e) H_3O^+, and f) CD^+.

The yields of selected cations produced from the ESD of Si(111)-(7×7):C_2D_2 surface are shown as a function incident electron energy in Figure 4.4. Each data point corresponds to the integrated peak area of the respective mass peak and normalized to the electron beam current.

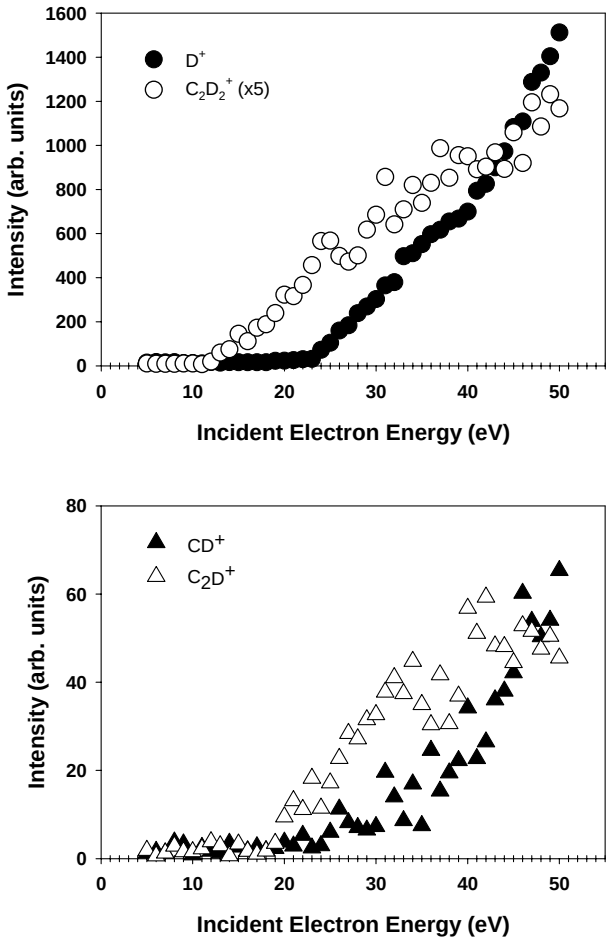

Figure 4.4: The top frame displays the yields of D^+ (filled circles) and $C_2D_2{}^+$ (open circles) from the ESD of acetylene-d_2 adsorbed on Si(111)-(7×7) as a function of incident electron energy. The $C_2D_2{}^+$ curve is multiplied by a factor of 5 to facilitate comparison of the ion yield curve shapes. The bottom frame presents the yields of the acetylene fragments CD^+ (filled triangles) and C_2D^+ (open triangles). All data has been normalized to the electron beam current.

The appearance threshold for D^+ occurs at an energy of 24–25 eV. Following the onset of desorption, the yield increases monotonically with increasing incident electron energy. The threshold energy at 24 eV and monoenergetic nature of the D^+ yield following the onset of desorption is consistent with proton desorption yields resulting from the ESD of hydrocarbons [75]. The molecular ion, $C_2D_2{}^+$, has a threshold energy of 12–13 eV. The $C_2D_2{}^+$ signal increases after the onset of desorption until 24 eV, where the plateaus briefly before decreasing at 26 eV. After 28 eV, the yield increases with the incident electron energy.

The ion intensities of the higher mass fragments produced from the ESD of Si(111)-(7×7):$C_2D_2{}^+$ were very small in comparison to those of the proton and molecular ion. Despite this, it was possible to determine the threshold energies for CD^+ and C_2D^+. The onset of desorption for CD^+ occurs at 24–25 eV, while the C_2D^+ ion first appears at 20–21 eV. At slow incident electron energies in particular, it is difficult to distinguish appreciable ion signal from the noise, therefore, the threshold energies of CD^+ and C_2D^+ may be closer to each other than the 4–5 eV energy difference infers.

4.4 Discussion

4.4.1 D^+ Appearance Threshold

The production and desorption of positively charged species from a surface typically involve the creation of two-hole states. For D^+, a two-hole state is produced from the initial excitation of the C 2*s* shell of the acetylene molecule. The C 2*s* level has an ionization energy of 23–25 eV, which correlates with the appearance threshold of D^+. When the acetylene molecule is bombarded with an electron with sufficient kinetic energy to eject an electron from the C 2*s* level, Auger decay occurs resulting in two-hole final states. These two-hole states lead to Coulomb explosion and subsequent desorption of the deuterium cation. This excitation of the C 2*s* level is a widely accepted mechanism for proton desorption from various hydrocarbons [75–77]. Figure

4.5 illustrates this mechanism schematically.

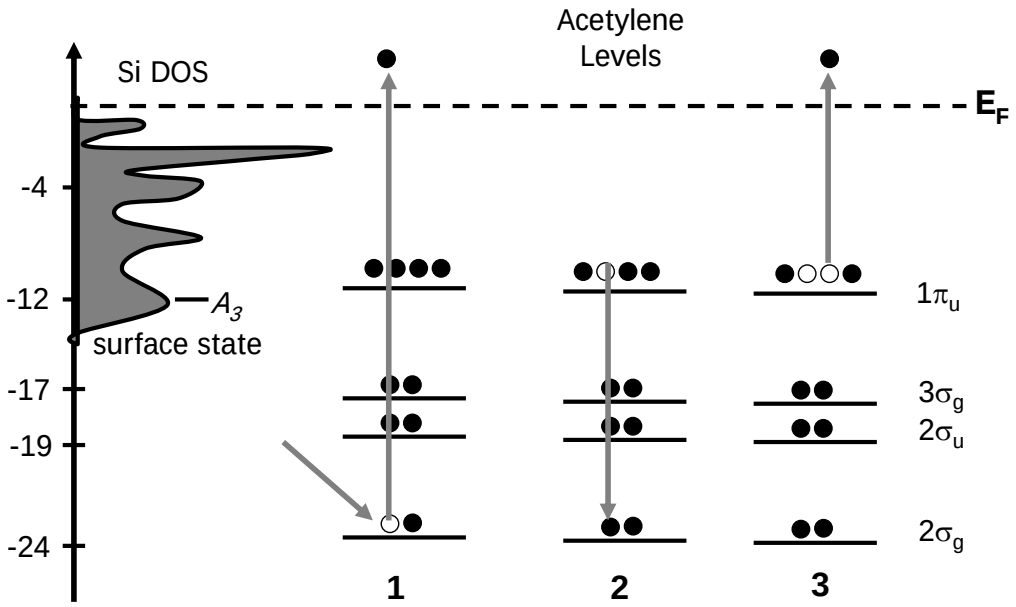

Figure 4.5: Illustration of the desorption mechanism of D^+ from ESD of acetylene adsorbed on Si(111)-(7×7). Step 1 depicts the initial excitation of the C 2*s* (or 2σg) level of the acetylene molecule by the incident electron. Step 2 shows Auger decay of an electron from a shallow level into the C 2*s*. Step 3 shows the ejection of the Auger electron, resulting in two holes localized at the shallow level.

4.4.2 $C_2D_2^+$ Threshold

Positive ions generated from electron-stimulated processes are typically fragments of the adsorbed parent molecule. However, in the case of C_2D_2 adsorbed on Si(111)-(7×7), there is a significant contribution to the ESD cation signal from the parent ion $C_2D_2^+$. The threshold energy of acetylene cation is 12–13 eV. To assign this threshold energy, the interaction of the acetylene molecule with surface states of Si(111) must be taken into consideration. In this instance, it is convenient to visualize the Si(111)-(7×7):C_2D_2 complex as a molecule. An incident electron with 12–13 eV of kinetic energy is capable of ionizing the Si(111)-(7×7):C_2D_2 "molecule," likely producing a

hole in the π–R state of the complex. The π–R state is representative of the Si–C σ bond and ionization at this level results in a reduction in bonding character of Si–C bond. A hole localized at the π–R level would result in direct dissociation of the Si(111)-(7×7):C_2D_2 "molecule," producing $C_2D_2{}^+$.

Another possible mechanism leading to $C_2D_2{}^+$ desorption is the creation of a two-hole, one-electron state initiated from the ionization of the π–R state. As described in Chapter 3, the π–R state is created from the overlap of the $1\pi_u$ state of acetylene and the Si dangling bond states (A_3 surface state). Both the $1\pi_u$ and A_3 surface state have ionization potentials of 11–12 eV, so it is expected that the π–R state will have an ionization potential slightly higher than that. Calculations place the π–R level ∼11–12 eV [126]. When an incident electron with sufficient kinetic energy ionizes the π–R level, Auger decay from the π^*–AD level can occur, resulting in two holes localized on that state. Subsequently, Coulomb repulsion takes place causing the ejection of $C_2D_2{}^+$. This Auger decay process would lead to $C_2D_2{}^+$ and not fragmentation into other species because the π^*–AD state also gives bonding character to the Si(111)-(7×7):C_2D_2 complex. Therefore, bond cleavage would be localized at the Si–C bond. A schematic of this Auger decay mechanism is shown in Figure 4.6.

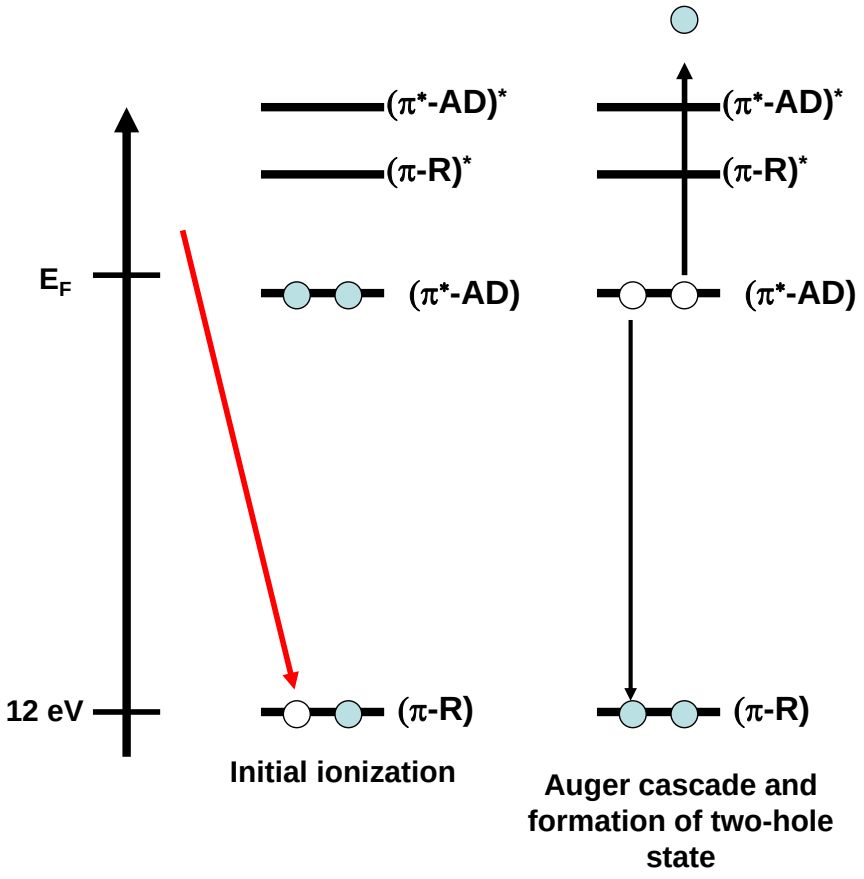

Figure 4.6: Schematic of the desorption mechanism of $C_2D_2^+$ from ESD of acetylene adsorbed on Si(111)-(7×7) due to Auger decay. Bombardment of the complex with 12–13 eV electrons results in the ejection of an electron localized in the π–R level. Auger cascade occurs as an electron from the π^*–AD level fills the hole, causing ejection of the other electron in the π^*–AD level. The two-hole state Coulomb explodes, leading to desorption of $C_2D_2^+$.

4.4.3 Resonance Structure in the $C_2D_2^+$ Spectrum

After the onset of desorption at 12–13 eV, the $C_2D_2^+$ signal increases to 24 eV where it plateaus briefly and then decreases sharply from 26–27 eV. The structure in this region can be attributed contributions from excitations of the Si 3*s* level of the silicon atom. The Si 3*s* level has an ionization potential of 21–23 eV [78].

4.4.4 Threshold Energies of Hydrocarbon Fragments

The electron bombardment of C_2D_2 on Si(111)-(7×7) results in the production and release of hydrocarbon fragments. The CD^+ ion threshold energy is 24–25 eV and the C_2D^+ appearance threshold occurs at 20–21 eV. At very low electron energies, it is difficult to distinguish the signal from the noise, and therefore the CD^+ and C_2D^+ threshold energies may be closer in energy to each other than the data shows. However, it is possible that for CD^+, the 24–25 eV desorption yield can be attributed to first cleavage of one Si–C bond of the di-σ bonded complex, followed by breakage of the C–C bond of the acetylene. The desorption of CD^+ would then be attributed to an excitation of the C $2s$ level after cleavage of the Si–C bond. The C $2s$ level lies at 24–26 eV, and this energy correlates closely with the CD^+ threshold energy. For C_2D^+, it may be possible that a similar sequential fragmentation occurs. In the case of C_2D^+, the C–C double bond may fragment first, followed by excitation of the Si $3s$ level resulting in desorption. The Si $3s$ level lies at 20–21 eV, and this energy correlates to the C_2D^+ threshold energy of 20–21 eV.

4.5 Conclusions

Acetylene adsorbed on the Si(111)-(7×7) surface is a complex adsorbate-substrate system. The interaction of low-energy electrons with this surface results in the production and release of ionic species including protons, hydrocarbon fragments, and the acetylene molecular ion. The appearance threshold of D^+ occurs at 24 eV, and the monotonic increase with incident electron energy is consistent with that of protons produced from the ESD of various hydrocarbons.

The hydrocarbon fragments, while a small contributor to the total ion signal, displayed threshold energies of 20–25 eV. Threshold energies in the range suggest primary cleavage of the Si–C or C–C bonds followed by excitation of either the C $2s$ level (24 eV) or the Si $3s$ level (20–21 eV) resulting in desorption of CD^+ and

C_2D^+. However, at these very slow incident electron kinetic energies, the ion signal is small, therefore it is difficult to assign the exact mechanism for fragmentation and desorption.

The ESD of Si(111)-(7×7):C_2D_2 also resulted in the production and emission of the molecular cation. While the appearance of the other ions can be explained by initial excitations, and subsequent Auger decay, of shallow core levels of either the C or Si atom, $C_2D_2{}^+$ desorption is attributed to the excitation of the silicon surface state.

CHAPTER V

ELECTRON-STIMULATED DESORPTION OF ATOMIC DEUTERIUM FROM DEUTERATED ACETYLENE ADSORBED ON THE SILICON(111) SURFACE

5.1 Introduction

When low-energy electrons collide with a surface, particularly an adsorbate-covered surface, the electrons scatter inelastically. These scattering processes may induce decomposition of the adsorbates on the surface into reactive fragment species which may result in the formation and desorption of neutral species. In the previous chapter, the electron-stimulated desorption of cations from acetylene adsorbed on the Si(111) surface was discussed. In this chapter, the desorption of neutral atomic deuterium from this adsorbate-substrate system as a result of low-energy electron bombardment is presented.

In order to detect the neutral deuterium, a technique known as resonance enhanced multiphoton ionization or REMPI was used. REMPI is a sensitive and selective method for detecting atoms and small molecules in the gas phase. REMPI involves the use of a tunable laser to access excited states of an atom or molecule. For (2 + 1) REMPI, an atom absorbs two photons, in which the sum of the energies is equal to that of the energy gap between to electronic levels of the species. The atom (or molecule) is then ionized by the absorption of an additional photon. The ejected photoelectron may be detected, or in the case of these experiments, the ion is detected with a time-of-flight mass spectrometer. The (2 + 1) REMPI detection scheme used for atomic deuterium is shown in Figure 5.1.

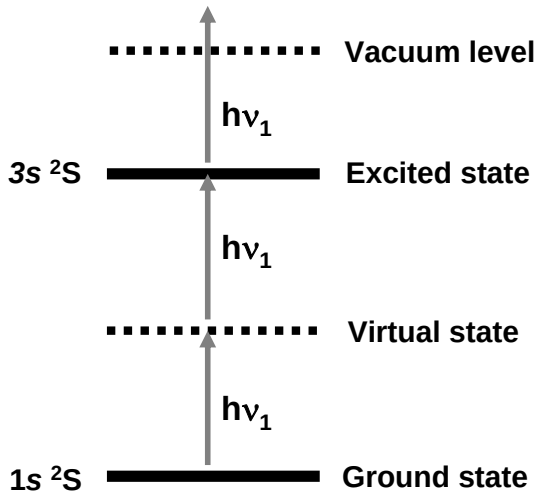

Figure 5.1: (2 + 1) REMPI detection scheme used for atomic deuterium D(^{2}S) from the ESD of acetylene-d_2 adsorbed on Si(111)-(7×7).

5.2 Experimental Details

The experiments were carried out in the same UHV apparatus described in Chapter 4. ESD threshold measurements were obtained by scanning the incident electron energy in 1 eV increments from 5 to 50 eV. An electron beam pulse width of 1 μs was used, which effectively integrates over the entire kinetic energy distribution. Cations generated from the electron bombardment of the surface were extracted by a negative potential pulse that was applied immediately following the electron beam pulse. The neutral fragments, which remain in their original desorbing trajectories with their initial kinetic energies, were detected by focusing a tunable, pulsed laser beam above and parallel to the surface. Neutral deuterium, D(^2S), was detected using a (2 + 1) REMPI (resonance enhanced multiphoton ionization) scheme. The two photon transition used for detecting D(^2S) was the $3s\ ^2S \leftarrow 1s\ ^2S$ transition at 205.048 nm. The laser wavelength required for this detection scheme was generated

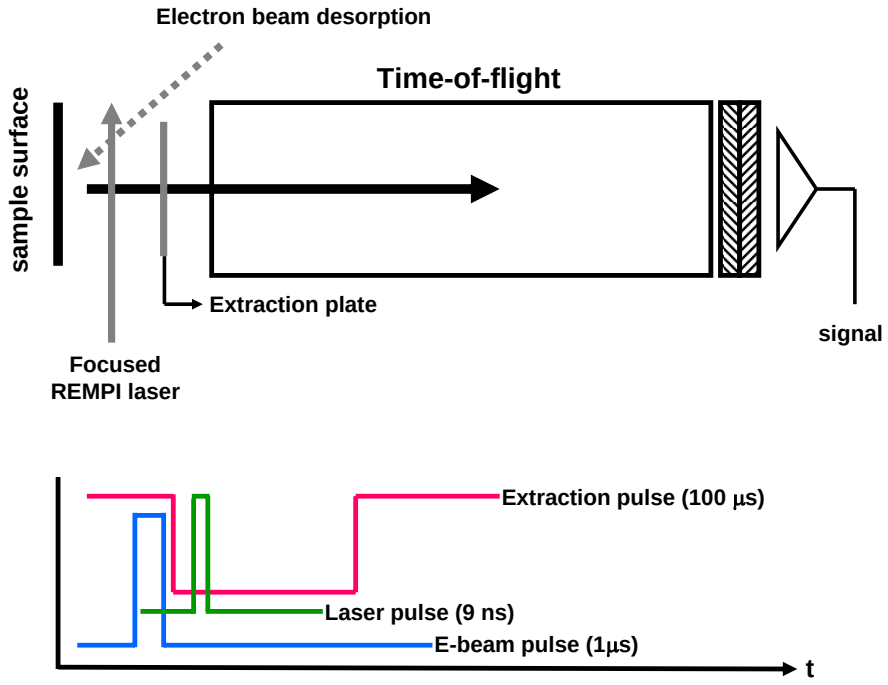

Figure 5.2: Diagram of the ESD-REMPI-TOF experiment with the pulse sequence used for detection of the neutral desorbates.

by frequency tripling the output of a Nd:YAG pumped dye laser with potassium dihydrate phosphate (KDP) and β-barium borate (β-BBO) crystals. Approximately 0.5 mJ/pulse of laser light was focused $\sim$1 mm over the silicon substrate. All data points correspond to the integrated area below each specific mass peak. Figure 5.2 illustrates the REMPI experiment and the pulse sequence used for detection of neutral species desorbed from the surface.

5.3 Results

5.3.1 Incident Electron Energy Dependence

The D(^{2}S) yield as a function of incident electron energy is presented in Figure 5.3. The onset of desorption for the deuterium atom occurs at 8 eV. From 8 eV to 12 eV the intensity plateaus and then increases sharply at 13 eV. The signal levels decreases

slightly at 14 eV and then increases monotonically with incident electron energy. The data is comprised of the average of several data sets, and the error bars at 8 eV, 13 eV and 14 eV verify the structure in the yield.

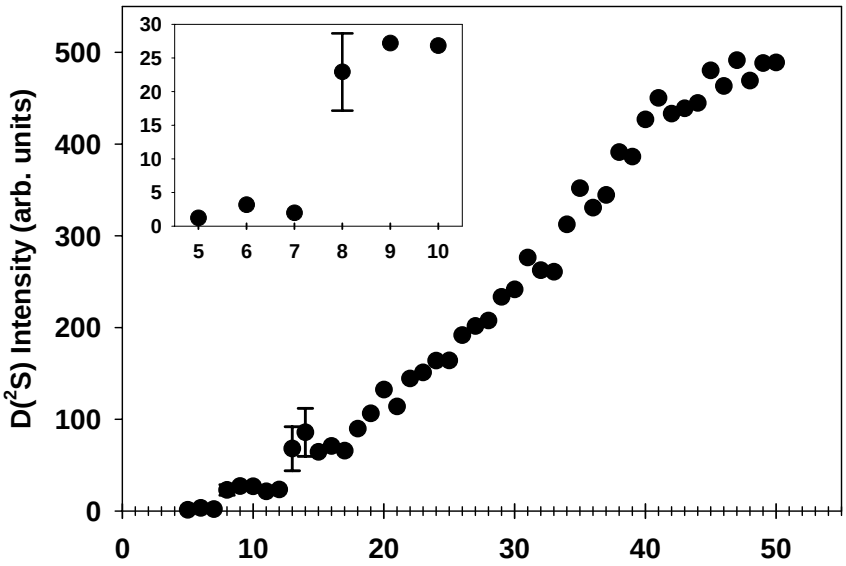

Figure 5.3: Plot of the neutral D(^{2}S) yield versus incident electron energy. The data was obtained by probing the D($3s$ ^{2}S $\leftarrow$ $1s$ ^{2}S) REMPI transition. The inset shows the low energy region of the spectrum. Error bars of selected data points verify the structure in the intensity.

5.3.2 Time-of-Flight Distributions

In order to determine the origin of neutral deuterium, and the possible mechanisms by which it desorbs, time-of-flight distributions were measured. The time-of-flight distributions were fit to the Maxwell-Boltzmann expression

$$I(t) = C_1 t^{-3} exp\left[-\frac{m}{2kT_1}\frac{d^2}{t^2}\right] + C_2 t^{-3} exp\left[-\frac{m}{2kT_2}\frac{d^2}{t^2}\right] \quad (2)$$

The fitting procedure to this Maxwell-Boltzmann expression has been previously described in [79]. The time-of-flight data is fit to multiple components where C_1 and C_2 are proportionality constants, T_1 and T_2 are the effective temperatures, m is the mass of the desorbing neutral fragment, d is the distance from the surface to the laser beam, k is the Boltzmann constant, and t is the delay time between the electron beam and laser beam. The time-of-flight distribution spectrum of $D(^2S)$ at incident electron energy of 50 eV is shown in Figure 5.4. The dotted line represents the thermal Maxwell-Boltzmann distribution with an effective temperature of 130 K. Dashed and dashed/dotted lines correspond to the highly energetic non-thermal component and the non-thermal intermediate component, respectively. At 50 eV, the $D(^2S)$ distribution is bimodal with a narrow, fast peak at 0.8 μs and a broad, slow peak at 2.6 μs. The fast, energetic component corresponds to a translational kinetic energy of 557 meV (4300 K). The intermediate non-thermal, with an effective temperature of 900 K, corresponds to a translational kinetic energy of 116 meV. The slow, thermal component has a translational kinetic energy of $\sim$17 meV.

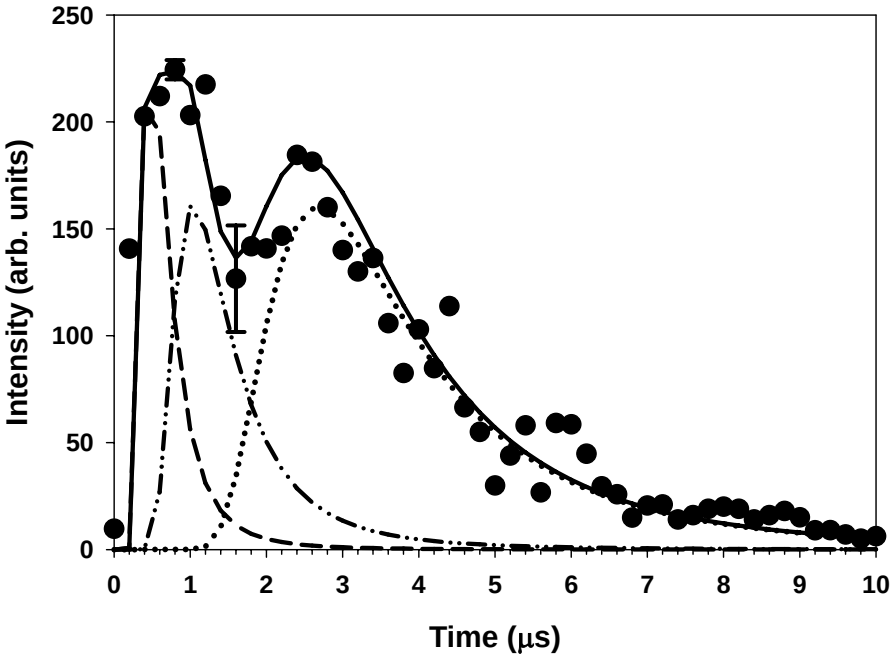

Figure 5.4: Summation of multiple Maxwell-Boltzmann distributions (solid line) fit to D(^{2}S) time-of-flight data taken at 50 eV. The dotted line represents the thermal Maxwell-Boltzmann distribution with an effective temperature of 130 K. The dashed and dashed/dotted lines represent a highly energetic non-thermal component and a non-thermal intermediate component, respectively.

5.4 Discussion

5.4.1 Appearance Threshold at 8 eV

The low-energy electron bombardment of Si(111)-(7×7):C_2D_2 results in the desorption of neutral atomic deuterium. The onset of desorption for D(^{2}S) occurs at an energy of 8 eV. In this energy regime, dissociative electron attachment resonances are accessible, opening up the possibility for the formation of neutral and anionic fragments from the parent molecule. These attachment resonances can produce energetically excited negative ion species which can then dissociate into neutral and negative ion fragments.

When the incident electron collides with the molecule, inelastic scattering can result in the in the promotion of an electron to a Rydberg level. For instance, an electron in the 1πu orbital can be promoted to an empty $3s\sigma_g$ orbital. The original incident electron can then be temporarily captured in empty antibonding or other valence or Rydberg levels, resulting in the formation of a core-excited negative ion resonance. This resonance is known as a one hole-two electron Feshbach resonance. This resonance can dissociate to form a neutral fragment and an anionic fragment.

For acetylene, two Rydberg states lie at energies near the 8 eV: 1) the $\tilde{C}\ ^3\Pi_u$ at 8.07 eV and 2) the 3R $^1\Pi_u$ at 8.16 eV [44, 80]. In the gas phase, these resonances have been shown to dissociate in the following ways:

$$C_2H_2 \rightarrow {C_2H_2}^{*-} \rightarrow C_2H^- + H$$
$$C_2H_2 \rightarrow {C_2H_2}^{*-} \rightarrow C_2^- + 2H$$

Both of these dissociation pathways lead to the formation of hydrogen (deuterium) atoms. Thus, at 8 eV, the formation of Feshbach resonances involving the $^1(\pi, 3s)$ and the $^3(\pi, 3s)$ Rydberg states are likely responsible for the appearance threshold for D(^{2}S).

5.4.2 Structure at 13–14 eV

The D(^{2}S) energy dependence spectrum reveals resonance structure in the 13–14 eV region. This resonance structure lies above the ionization potential of the acetylene molecule (11.5 eV). Thus, the feature at 13–14 eV could be due to dissociative ionic states of ${C_2D_2}^+$. Dissociation pathways include:

(i) $\quad {C_2D_2}^+ \rightarrow {C_2D}^+ + D$
(ii) $\quad {C_2D_2}^+ \rightarrow {C_2}^+ + 2D$
(iii) $\quad {C_2D_2}^+ \rightarrow {CD}^+ + C + D$
(iv) $\quad {C_2D_2}^+ \rightarrow C^+ + CD + D$

Several electron impact ionization studies of acetylene indicate the appearance potentials for these channels as follows: i) 17 eV, ii) 22 eV, iii) 24 eV, and iv) 25 eV [63,

67–71, 73, 81]. If the dissociation of $C_2D_2^+$ cation was involved, the likely pathway responsible for the resonance feature at 13–14 eV would be $C_2D_2^+ \rightarrow C_2D^+ + D$, with an appearance potential of 17 eV. This value correlates well with the appearance threshold of C_2D^+ reported in Chapter 4. Although this energy is close to the feature in the D(^{2}S) energy dependence spectrum, a 3 eV energy difference makes it difficult to assign this dissociation pathway as the source of the structure at 13–14 eV.

Another possible explanation for the feature at 13–14 eV is direct desorption of deuterium from Si atoms not involved in the di-σ bonding of acetylene. Although it has been determined that acetylene does not dissociate upon adsorption on Si(111)-(7×7), it is possible that background hydrogen (deuterium) may interact and bond with available Si dangling bonds. One possible mechanism for desorption of D(^{2}S) is the excitation of the A_3 surface state of Si(111)-(7×7). The A_3 surface state has an ionization potential of 11–12 eV. Desorption of D atoms from this surface state would involve ejection of an electron in the Si–D bond. The resulting 1 hole-1 electron state leads to desorption of neutral deuterium. In this energy range it is evident that both cationic and neutral species are formed due to electron bombardment, therefore, it is difficult to determine a dominant mechanism for the structure at 13–14 eV.

5.4.3 The D(^{2}S) Energy Distribution

Figure 5.4 presents the time-of-flight distributions for D(^{2}S) desorption at an incident electron energy of 50 eV. This energy is well above the ionization potential of acetylene, and as discussed in the previous section, there are several dissociative ionic states that can lead to the formation of D(^{2}S). The incident electrons may also scatter and generate low-energy secondary electrons, which can induce DEA reactions. However, it is important to note that 50 eV is still below the energy required for double ionization of acetylene. Thus, at an incident electron energy of 50 eV, it is possible to

sample both the low-energy induced reactions from interactions with scattered electrons and the surface, and the direct dissociative ionizations channels produced from fragmentation of $C_2D_2^+$.

The fast, non-thermal component of the time-of-flight distribution could not be fit to a single Maxwell-Boltzmann distribution. The requirement for multiple distributions to fit the fast component is likely due to the bonding geometry of di-σ bonded acetylene on Si(111)-(7×7). Figure 5.5 illustrates the angle dependence of the deuterium atoms on C_2D_2 di-σ bonded to the Si(111)-(7×7) surface. The desorption trajectory is quite different for the two deuterium atoms of the acetylene molecule in the di-σ conformation. Considering the distance from the surface to the REMPI laser is approximately 4 mm, the distance to the laser field for deuterium atom 1 is ∼4.4 mm. Deuterium atom 2 must travel more than twice the distance, approximately 9.5 mm, to reach the laser field. This dissimilarity in the distances traveled by the two D atoms is directly correlated to the flight time.

Geometrical considerations aside, the fast, non-thermal component at 0.8 μs corresponds to a translational kinetic energy of 557 meV. The second component of the non-thermal peak corresponds to a translational kinetic energy of 116 meV. The non-thermal region of the time-of-flight distribution is likely due to repulsive forces associated with DEA resonances and dissociative excited states.

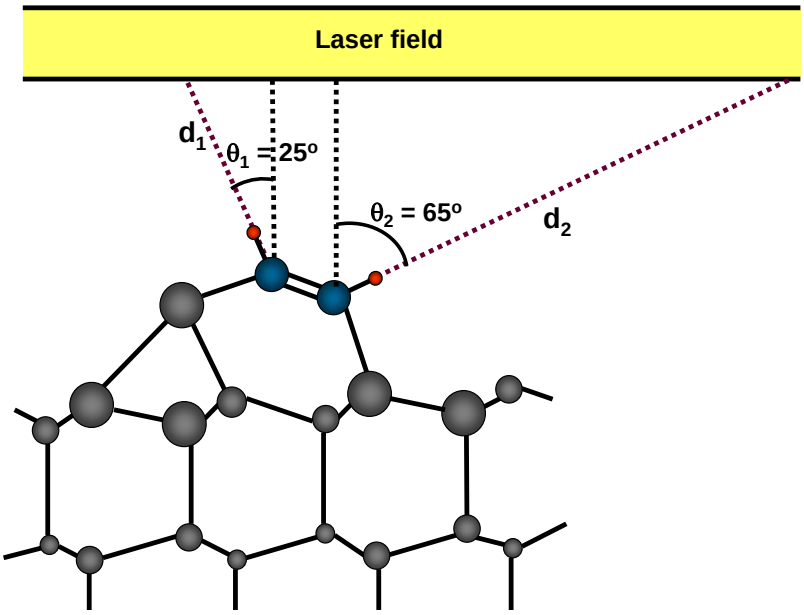

Figure 5.5: Schematic illustrating the probable desorption trajectories of deuterium atoms ejected from di-σ bonded acetylene on the Si(111)-(7×7) surface. The distance from the surface normal to the laser field is 4.0 mm. Deuterium atom 1 (on the left) is 25° off the surface normal, resulting in a distance, d_1, of 4.4 mm to the laser field. For deuterium atom 2 (on the right), the 65° offset from the surface normal results in a distance, d_2 of 9.5 mm to the laser field.

In instances where D(^{2}S) does not desorb directly from the surface following excitation, the departing deuterium atom may collide with the surface where it may thermalize and equilibrate to the surface temperature. Therefore, the thermal component of the time-of-flight distribution can be attributed to D atoms which are involved in collisions with the surface upon desorption.

At incident electron energy of 50 eV, D(^{2}S) can be produced from both dissociation of $C_2D_2^+$ and attachment resonances. For dissociation of the acetylene cation, gas phase studies [69] indicate the maximum translational kinetic energy involved in the production of C_2H^+ is 400 meV. This is quite lower than the translational kinetic energy of the non-thermal component presented in this chapter. However, 400 meV corresponds to C2H+ produced from bombardment with 24 eV electrons. It may be

possible that excess kinetic energy in our measurements may be due to the higher kinetic energy of the incident electrons.

5.5 Conclusions

In this chapter, it has been shown that $D(^2S)$ is a produced from electron-stimulated processes on the Si(111)-(7×7):C_2D_2 surface. REMPI, in conjunction with ESD-TOF-MS, is a sensitive and selective tool that allows for the state-resolved detection of emitted deuterium atoms. Threshold data indicates multiple source terms for the production of $D(^2S)$. In the low-energy regime, the dissociation of Feshbach resonances originating from Rydberg states of the acetylene molecule, are responsible for the onset of desorption of deuterium atoms at 8 eV. At incident electron energies above the ionization threshold of acetylene, dissociation of $C_2D_2^+$ is attributed to the production of $D(^2S)$ at higher energies. Time-of-flight distributions confirm multiple pathways for the creation of $D(^2S)$ from the ESD of this adsorbate-substrate system. These studies may provide insight into the dehydrogenation of organic layers adsorbed on silicon substrates by low-energy electrons.

CHAPTER VI

LOW-ENERGY ELECTRON INTERACTIONS WITH EPITAXIAL GRAPHENE ON SILICON CARBIDE (0001)

6.1 Introduction

Carbon-based materials, particularly those comprised of sp^2 hybridized carbon, have garnered much attention from the scientific community in recent years. Perhaps the most universally known sp^2 carbon material is graphite, a three-dimensional array of hexagonal carbon atoms. In 1985, its zero-dimensional counterpart, fullerene, was discovered by Curl, Kroto, and Smalley [82]. A few years later, the one-dimensional form known as carbon nanotubes was discovered [83]. The precursor for all of these allotropes is graphene. Structurally, graphene is described as a one-atom-thick, planar, hexagonal sheet of sp^2 hybridized carbon atoms. Despite the simplicity of its chemical structure, graphene was not discovered experimentally until 2004 [84]. Graphene was first isolated by applying sticky tape to peel individual graphene layers from highly oriented pyrolytic graphite (HOPG) in a process called micromechanical exfoliation. Graphene derived from this method displays intriguing electronic properties such as high electron mobility and ballistic transport of electrons [85]. Although micromechanical exfoliation provides high-quality graphene crystallites suitable for laboratory experiments, it is not a feasible method for generating graphene on the scale necessary for industrial purposes. Consequently, a scalable method for the production of graphene is desirable.

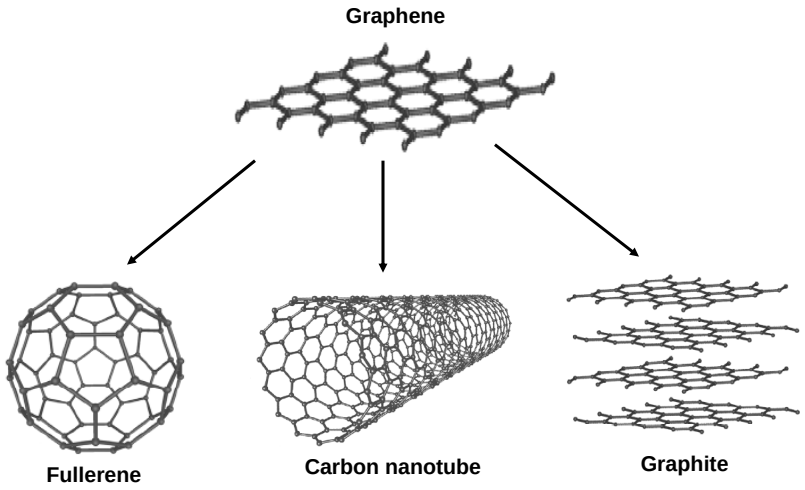

Figure 6.1: Structures of the sp^2 hybridized allotropes of carbon.

Several techniques have been developed to produce graphene including the chemical vapor deposition of graphene on metallic substrates from a carbon-containing precursor gas [86], exfoliation and reduction of graphite oxides [87–89], and Si sublimation from 6H-SiC single crystals [90]. The latter method produces films of epitaxial graphene of varying thicknesses depending on the polarity of the 6H-SiC substrate [91]. The Si-face, or SiC(0001) orientation, produces ultrathin (0–5 layers) of graphene. The C-face, or SiC($000\bar{1}$) orientation, yields few-layer graphene ($\geq$ 10 layers).

Since graphene has the potential to revolutionize the electronics industry by replacing Si- and CMOS-based technologies, it is important to develop strategies for large-scale patterning of this material. Standard lithographic techniques often employ electron beams to remove material from the surface of electronic materials, thus it is of technological and scientific importance to study the interactions of electrons with graphene. In this chapter, a detailed description of the interaction of low-energy electrons (5–50 eV) with ultrathin epitaxial graphene on SiC(0001) is discussed. ESD of cations and the effects of sustained electron-beam irradiation are reported in terms

of appearance threshold energies and removal cross sections, respectively.

6.2 Experimental Details

The epitaxial graphene samples were prepared by Nikhil Sharma of the School of Physics at the Georgia Institute of Technology. Before graphitization, a 6H-SiC(0001) substrate was etched in an RF furnace under a H_2:Ar (1:9) atmosphere at 1500 °C. The etched 6H-SiC(0001) crystal was then transferred to a UHV chamber equipped with an electron-bombardment heater and was annealed at 1200 °C resulting in the sublimation of Si atoms and graphitization of the terminal layers of the SiC(0001) surface. The epitaxial graphene sample probed in the ESD experiments was 3–5 layers thick. ESD experiments were carried out in the same UHV system described in Chapter 4. Electron energy dependence measurements were obtained by scanning the incident electron energy from 5–50 eV in 1 eV increments. The electron pulse width was 1 μs and the emitted cations were detected with a time-of-flight mass spectrometer. The electron fluence dependence measurements were obtained by irradiating the epitaxial graphene sample with a continuous beam of 50 eV electrons in 60 second intervals for the duration of 3600 seconds. Following every 60 second bombardment cycle, an ESD-TOF mass spectrum was collected. The experiments were conducted at room temperature.

6.3 Results

6.3.1 Electron-Stimulated Desorption of Cations from Epitaxial Graphene on SiC(0001)

Presented in Figure 6.2 is the ESD-TOF mass spectrum of epitaxial graphene grown on SiC(0001). The most prominent feature in the spectrum is the H^+ peak. The other peaks, largely hydrocarbon fragments, are multiplied by a factor of five for ease of comparison. The incident electron energy was 50 eV.

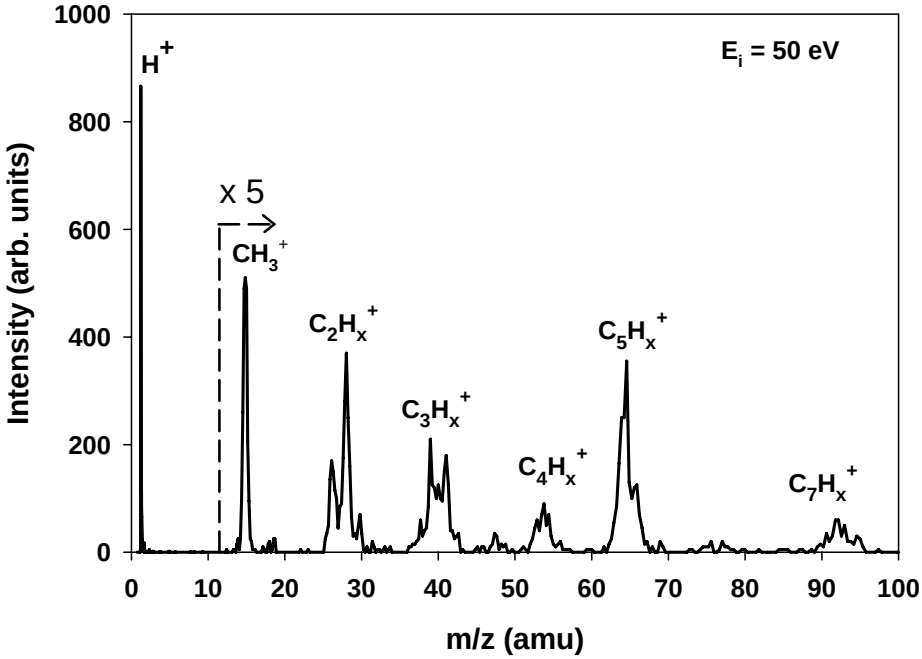

Figure 6.2: A typical ESD-TOF mass spectrum of cations emitted from epitaxial graphene on SiC(0001) from bombardment with 50 eV electrons. The higher mass peaks are multiplied by a factor of five for ease of comparison.

The electron-stimulated desorption of H^+ and selected hydrocarbon fragments are presented in Figure 6.3. The onset of desorption for H^+ and $CH_3{}^+$ occurs at an energy of 20–21 eV for both cations. The threshold energies of $C_3H_x{}^+$, $C_5H_x{}^+$ and the other high mass hydrocarbon fragments are 24–25 eV. Following the onset of desorption, cation yields as a function of incident electron energy increase monotonically, and this behavior is displayed for all desorbates.

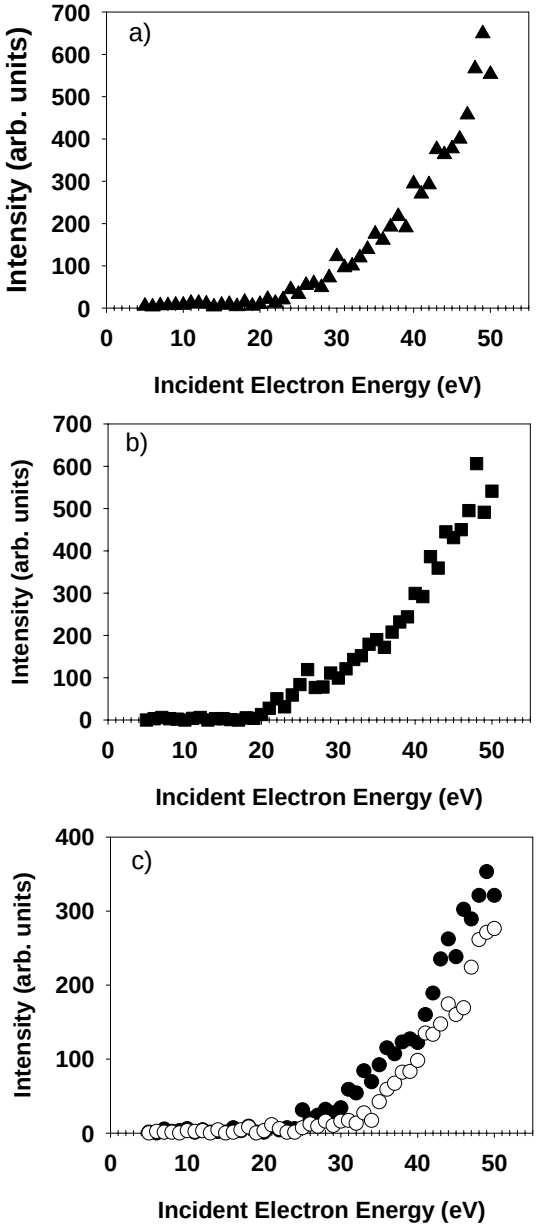

Figure 6.3: Cation yields produced from ESD of epitaxial graphene as a function of incident electron energy. In frame a) H^+, b) $CH_3{}^+$, and c) $C_3H_x{}^+$ (filled circles) and $C_5H_x{}^+$ (empty circles). Each data point is representative of the corresponding mass peak area. Data are normalized to the electron beam current.

6.3.2 Cation Desorption Yields as a Function of Electron Fluence

In order to understand the effects of prolonged electron bombardment on epitaxial graphene, electron fluence dependence measurements were conducted. The yields of cations ejected due to the ESD of epitaxial graphene are plotted as a function of electron fluence in Figure 6.4. Each data point corresponds to the integrated area below the specific mass peak. The CH_3^+, $C_3H_x^+$, and $C_5H_x^+$ data are normalized to the H^+ signal intensity at t_0. With increasing electron fluence, the cation yields decay exponentially. However, it is important to note that the H^+ and CH_3^+ yields do not decay to zero. The hydrocarbon fragments decay to values which are essentially the baseline signal as determined by the detection limits of the time-of-flight spectrometer.

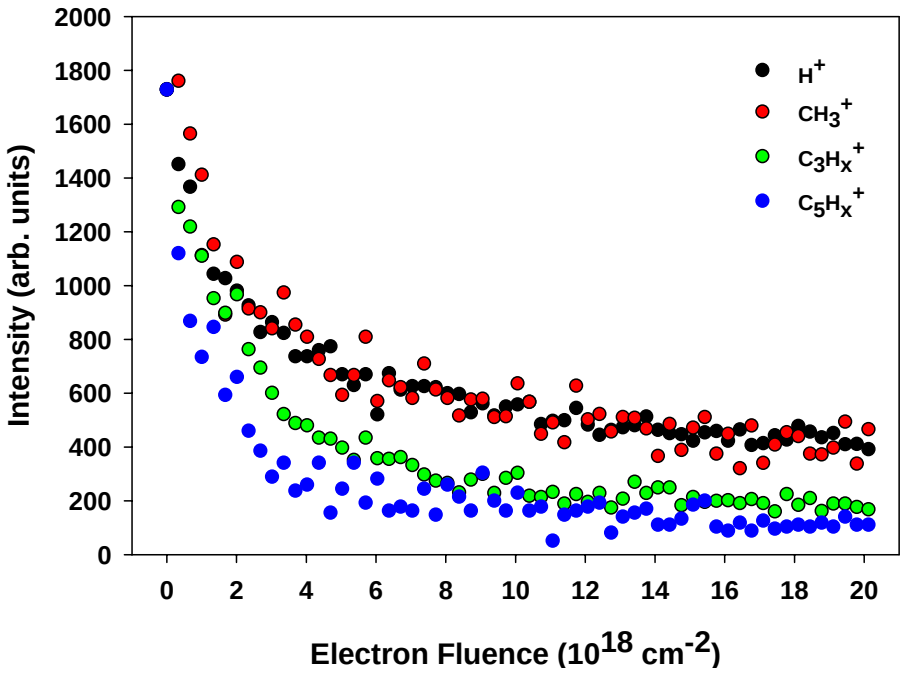

Figure 6.4: The yields of H^+ (black circles), CH_3^+ (red circles), $C_3H_x^+$ (green circles) and $C_5H_x^+$ (blue circles) plotted as a function of electron dose. The CH_3^+, $C_3H_x^+$, and $C_5H_x^+$ data were normalized to the H^+ intensity at t = 0.

6.4 Discussion

6.4.1 Appearance Threshold Energies of Cations

Although graphene is a continuous network of carbon atoms, its edges are terminated by hydrogen atoms. Therefore, the likely source of H^+ from ESD of epitaxial graphene is the edge sites. However, the surface of epitaxial graphene on SiC(0001) is quite rough, exposing underlying layers of graphene and the SiC substrate [91]. Hence, the SiC substrate itself may also be a source of protons, especially considering the surface is etched with hydrogen before graphitization. So, for proton desorption, one must consider not only the obvious C–H bond cleavage, but also Si–H bond cleavage from the hydrogen-terminated Si-face of SiC(0001).

The onset of desorption for H^+ occurs at 21 eV. This threshold energy is near the value for proton desorption from various hydrocarbon surfaces (23–25 eV). In these cases, C–H is the source of H^+ and the production and desorption from this bonding site is created from excitations of the C $2s$ level, followed by Auger decay to form localized two-hole states leading to Coulomb repulsion [75]. The threshold energy of 21 eV is also in a good agreement with H^+ desorption from hydrogen-terminated Si surfaces and Si-terminated SiC [78, 92]. The mechanism leading to desorption for the Si–H bonding site is due to an initial excitation of the Si $3s$ level, followed by Auger decay and Coulomb explosion [78].

The methyl cation appearance threshold is also 20–21 eV. The origin of CH_3^+ is likely fragmentation of the graphene, however, one cannot rule out the possibility of methyl-terminated edge sites for epitaxial graphene. As with the H^+ desorption, the CH_3^+ threshold energy is attributed to excitation and Auger decay from the C $2s$ level. The other hydrocarbon fragments, $C_3H_x^+$ and $C_5H_x^+$ (as well as the other $C_nH_x^+$ fragments) have appearance threshold energies at 24–25 eV. These heavier fragments are produced from the electron bombardment-induced fragmentation of the epitaxial graphene. The threshold energies for the hydrocarbon fragments are in good

agreement with cation desorption from branched alkanes and other hydrocarbons [75–77]. The C–C bond cleavage, and subsequent ion desorption, are created from excitations of the C $2s$ level (at 24–26 eV) and the formation of two-hole states due to Auger decay, leading to Coulomb repulsion and cation desorption.

6.4.2 Behavior of Cations as a Function of Electron Fluence

As discussed in Chapter 1, the interaction of electrons with surfaces, particularly technologically relevant surfaces, is an important topic in terms of fundamental and applied science. The electron beam patterning of graphene for devices [93] is already underway, therefore it is imperative to investigate the effects of prolonged electron bombardment with this surface.

At incident electron energies as low as 20 eV it is possible to remove material from epitaxial graphene. Upon irradiation with 50 eV electrons over a period of one hour, the yields of the cation desorbates decreases exponentially with increasing electron fluence. It is important to note that, even at UHV pressures, background water is present in the chamber. Consequently, over the course of the experiment, the H3O+ yield increased.

The cross section for the electron-stimulated desorption of cations from graphene oxide deposited on Si(100) was calculated from the data in Figure 6.4 from the equation

$$\frac{n(t)}{n_0} = exp\left[-\left(\frac{JQ}{e}\right)\cdot t\right] \tag{3}$$

where n is the number of adsorbed species, J is the current density and Q is the cross section. The cross sections for selected cations are listed in Table 6.1.

Table 6.1: Removal cross sections for selected cations emitted from ESD of epitaxial graphene on SiC(0001) at 50 eV.

Ion	Cross section ($\times 10^{-19}$ cm^2)
H^+	2.15
$CH_3{}^+$	2.01
$C_3H_x{}^+$	0.71
$C_5H_x{}^+$	1.13

The effective cross section for cation removal from electron-stimulated desorption of epitaxial graphene on SiC(0001) at 50 eV is 2.6×10^{-19} cm^2.

6.5 Conclusions

The remarkable electronic properties of graphene have made it the leading candidate to replace Si and CMOS electronics. Electron-stimulated desorption of epitaxial graphene on SiC(0001) results in the production and emission of proton, methyl cation, and hydrocarbon fragments. The onset of desorption for these cations ranges from 20–25 eV. The mechanism for desorption can be assigned to the creation of two-hole states formed by Auger decay from either the C 2s or Si 3s shallow core levels. The close proximity of the two-holes leads to Coulomb explosion and the ejection of positively charged species from the surface.

With increasing electron dose, cation yields decrease exponentially. The removal cross sections of cations range from 7×10^{-20} cm^2 to 2×10^{-19} cm^2. In particular, the high removal cross section for H^+ indicates facile removal from edge sites, however the contribution from the hydrogen-terminated SiC(0001) substrate cannot be disregarded.

CHAPTER VII

LOW-ENERGY ELECTRON INTERACTIONS WITH GRAPHENE OXIDE FILMS ON SILICON(100)

7.1 Introduction

As the motivation for reproducible, inexpensive growth strategies for graphene continues to intensify, traditional synthetic chemistry approaches have emerged as an appealing alternative to methods that require vacuum pressures or clean room facilities. One promising precursor for graphene is graphite oxide. Graphite oxide was first synthesized by Brodie in 1857 by treating graphite with potassium chlorate and fuming nitric acid [94]. In 1957, Hummers et al. synthesized graphite oxide by treating graphite with a mixture of sulfuric acid (H_2SO_4), sodium nitrate ($NaNO_3$), and potassium permanganate ($KMnO_4$) [95]. Exposure to these strong oxidizing agents leads to intercalation of oxygen-containing species into the graphite lattice. Although graphite oxide has been synthesized for over 150 years, its exact chemical structure is still undetermined. Several structural representations have been proposed by theoretical predictions [96, 97] and various experimental techniques [88, 98–108]. The consensus is that upon oxidation, graphite oxide retains much of the original graphite structure, a hexagonal array of sp^2 hybridized carbon atoms, with epoxide and hydroxyl groups above and/or below the basal plane and carboxyl and alkyl groups terminating the edges. Due to the insertion of the epoxide and hydroxyl groups within the basal plane, the interlayer distance of graphite oxide is expanded to ∼10 Å. A schematic model of graphite oxide is presented in Figure 7.1 [109].

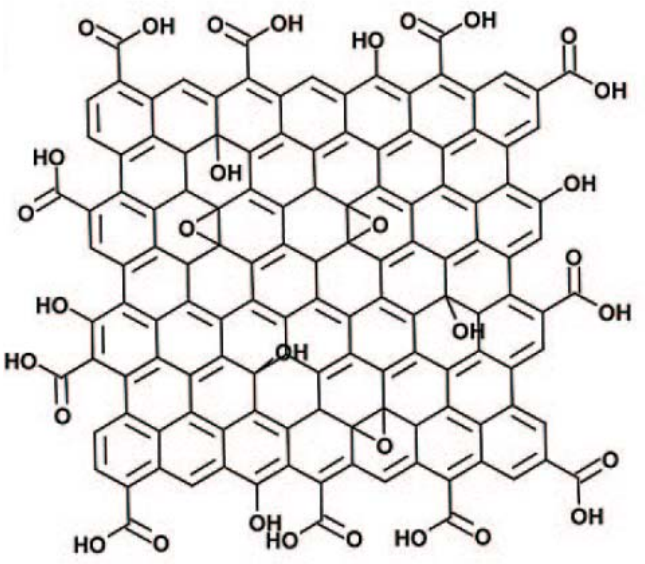

Figure 7.1: Structural model of graphite oxide [109].

Unlike graphite, graphite oxide is soluble in water, and therefore can be easily exfoliated into individual layers to form *graphene* oxide. Once graphene oxide layers have been isolated, they can be deposited onto substrates followed by reduction to graphene. Several techniques have been attempted to reduce graphene oxide. Thermal reduction of graphene oxide requires temperatures approaching 1100 °C [88, 110–113]. However, thermal annealing does not result in complete reduction. Although the annealed films gain some conductivity, their electrical properties are inferior in comparison to graphene. Reduction of graphene oxide via chemical exposure is also a widely used pathway to graphenic films [87, 89, 110, 112, 114–122]. Chemical reduction of graphene oxide typically involves exposing the material to hydrazine (N_2H_4). However, similar to the films produced from thermal annealing, complete reduction is not achieved. Additionally, nitrogen atoms are incorporated into the graphene oxide lattice.

In this chapter, a detailed study of the interaction of low-energy electrons with

graphene oxide films deposited on Si(100) is discussed. The time-of-flight mass spectrum of the desorbates generated by electron impact is reported. The low-energy electron-stimulated desorption of cations from this adsorbate/substrate system was investigated, particularly focusing on the measurement threshold energies. Additionally, the cation desorption yields as a function of electron dose were examined, as well as the Auger electron spectra of graphene oxide prior to and after electron bombardment. The viability of low-energy electron bombardment as a strategy to reduce graphene oxide to graphene is discussed.

7.2 Experimental Details

Graphite oxide was synthesized from graphite powder (325 mesh, Alfa Aesar) using the modified Hummers method [95]. Exfoliation of graphite oxide was attained by dilution of 5% graphite oxide with deionized water followed by sonication for 30 minutes. The colloidal dispersion was centrifuged for 30 minutes. The resulting liquid phase, which contained mostly monolayer graphene oxide flakes, was isolated. A polished Si(100) wafer (n-type) was etched with 5% hydrogen fluoride and concentrated nitric acid. Following etching, the Si(100) wafer was thoroughly rinsed with deionized water and allowed to dry under flowing nitrogen. The silicon wafer was dip coated in the graphene oxide suspension. Atomic force microscopy (AFM) confirmed the deposition of single monolayers of graphene oxide flakes.

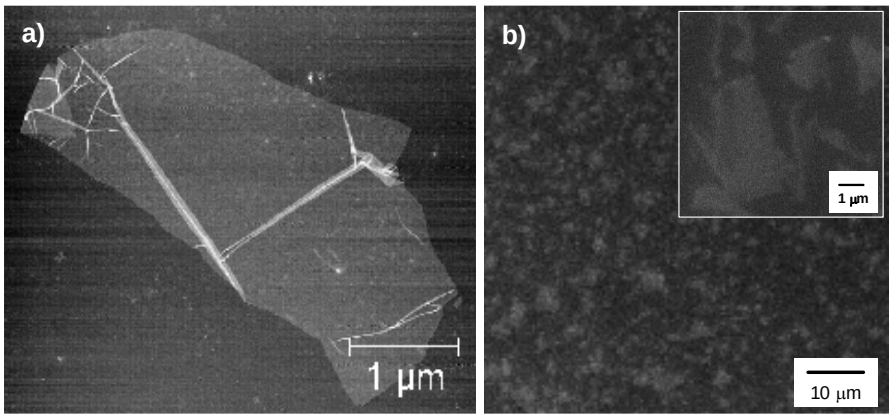

Figure 7.2: a) AFM and b) SEM images of graphene oxide flakes deposited on Si(100). The preparation of the graphene oxide samples and acquisition of the AFM and SEM images by Denis Sokolov, GIT.

The graphene oxide/Si(100) sample was mounted in the UHV chamber described in Chapter 4. In order to obtain threshold measurements, the ESD of cations was measured by scanning the electron energy from 5–50 eV in 1 eV increments. To maximize collection efficiency, the sample was grounded and a -255 V, 100 μs extraction pulse to the time-of-flight mass spectrometer entrance grid immediately following every electron pulse. Short electron pulses of 1 μs were used to minimize charging of the substrate and a frequency of 500 Hz allowed for complete discharge between pulses.

The yield as a function of electron dose measurements were obtained by irradiating, in continuous wave mode, the graphene oxide:Si(100) surface at incident electron energy of 50 eV for 60 seconds. Immediately following electron bombardment, an ESD-TOF-MS was obtained. The 60 second irradiation-ESD-TOF-MS sequence was repeated to a total irradiation time of 3600 seconds. Auger electron spectra of the substrate were taken before and after electron irradiation. Both the ESD and AES

measurements were taken at room temperature.

7.3 Results

7.3.1 Electron-Stimulated Desorption of Cations from Graphene Oxide on Si(100)

The time-of-flight mass spectrum of graphene oxide deposited on Si(100) is presented in Figure 7.3. Electron impact with this surface results in the production and desorption of several cations including protons, hydroxonium ions, hydrocarbon fragments, and oxygen-containing fragments. The dominant species desorbed from this surface are H^+ and the oxygen-containing fragment HCO^+.

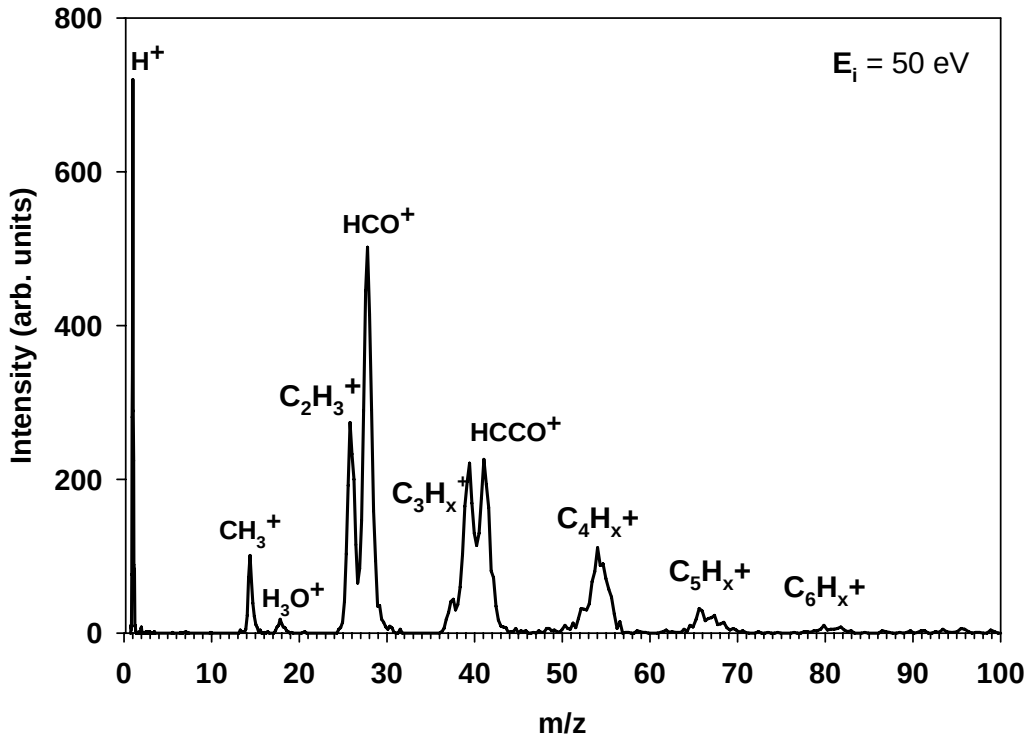

Figure 7.3: A typical ESD-TOF mass spectrum of cations emitted from graphene oxide deposited on Si(100) under the irradiation of 50 eV electrons.

The electron-stimulated desorption of selected cationic products as a function of incident electron energy are presented in Figure 7.4. For H^+, the onset of desorption occurs at 20 ($\pm$1) eV. Above 20 eV, the H^+ desorption yield increases linearly as a function of the incident electron energy. The oxygen-containing fragments, HCO^+ and $HCCO^+$ both have threshold energies of 18–19 ($\pm$1) eV. As with the H^+ yield, the desorption yields of HCO^+ and $HCCO^+$ increase linearly after the onset of desorption. The hydrocarbon fragments, $CH_3{}^+$ and $C_3H_4{}^+$ have threshold energies at 20 ($\pm$1) eV and their yields also increase linearly as a function of the incident electron energy following the onset of desorption. The other ions, $C_{2-6}H_x{}^+$, all have threshold energies at 20 eV and possess similar post-threshold behavior.

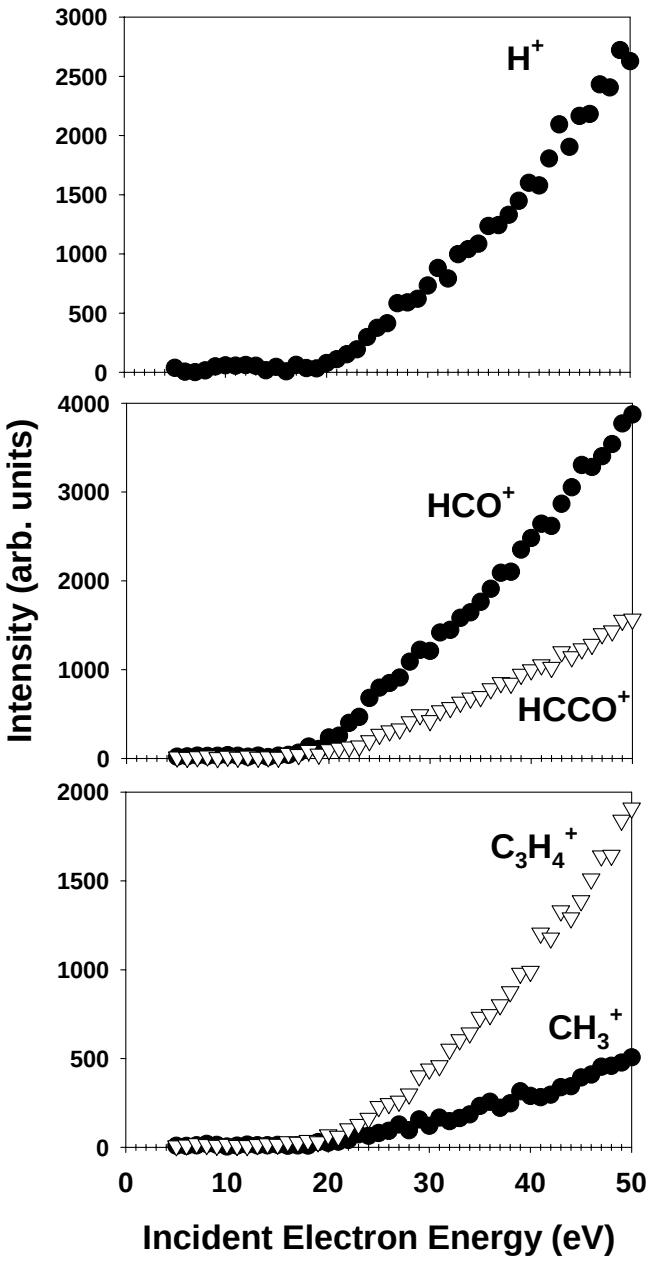

Figure 7.4: ESD cation yields as a function of incident electron energy. Each data point is representative of the corresponding mass peak area. The data are normalized to the electron beam current.

7.3.2 Cation Desorption Yields as a Function of Electron Fluence

The yields of selected cations as a function of electron dose are presented in Figure 7.5. Each data point is representative of the peak area of its respective mass and the data are normalized to the H+ signal intensity at t_0. As the electron fluence increases, the ion yields decay exponentially. It is important to note that the H^+ yield does not decay to zero, however, the yields of the other cations decay to values which are essentially the baseline signal as determined by the detection limits of the time-of-flight spectrometer.

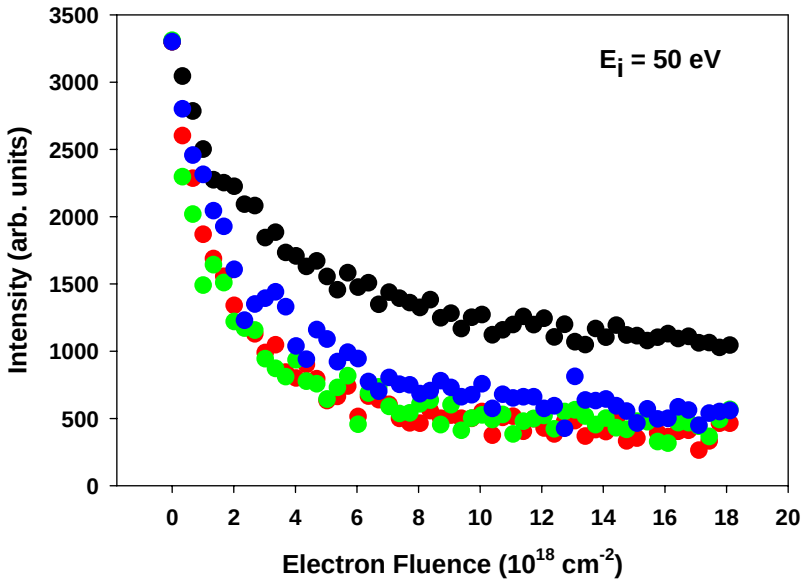

Figure 7.5: The yields of H^+ (black circles), HCO^+ (red circles), $HCCO^+$ (green circles) and $C_2H_3^+$ (blue circles) as a function of electron dose. The HCO^+, $HCCO^+$, and $C_2H_3^+$ data were normalized to the H^+ signal intensity at t = 0.

7.3.3 Auger Electron Spectra of Pre- and Post-irradiated Graphene Oxide Films

The Auger electron spectra of the graphene oxide/Si(100) substrate before and after electron bombardment are shown in Figure 7.6.

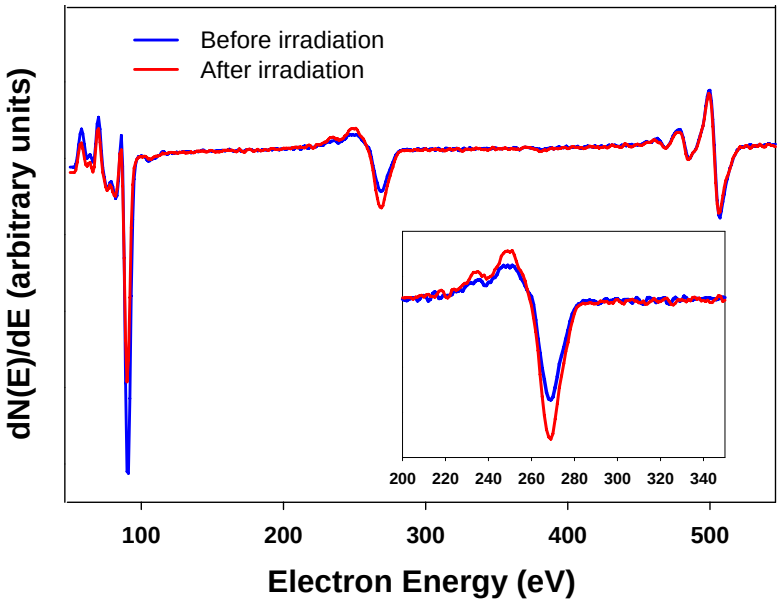

Figure 7.6: Auger spectra of graphene oxide deposited on Si(100) before (blue curve) and after (red curve) bombardment with 50 eV electrons (total fluence $\sim 20 \times 10^{18}$ cm^{-2}). The inset shows the C KLL region.

Both spectra show evidence of the underlying Si(100) substrate with the Si LVV feature at 90 eV. The other prominent features, the carbon KLL and oxygen KVV, are present in both spectra. Although the ESD data shows oxygen-containing functional groups are removed by electron bombardment, the oxygen AES peak for the post-irradiated surface remains largely unchanged. However, it should be noted that the underlying silicon surface may have been oxidized, to some extent, during the graphene oxide dip coating procedure. Therefore, the Si(100) surface may be contributing

the O KVV signal. As discussed in Chapter 2, the carbon KLL region of an Auger spectrum can reveal information regarding the morphology of carbonaceous material. The main minimum in the C KLL peak is at 268 eV for both spectra, and for the post-irradiated film, is higher in intensity. This is similar to the main minimum C peak for the CVD film described in Chapter 2. Typically, the main minimum for sp^2 carbon materials is at 272 eV. This shift to lower energy for the graphene oxide (and partially oxidized CVD film) may be indicative of oxygen-containing carbon materials [123, 124]. The satellite peaks of the post-irradiated film are higher in intensity, but the shapes of both spectra are similar. The satellite peaks are comprised of a small maximum at 248 eV, immediately followed by a weak minimum at 239 eV and a small maximum at 234 eV. This pattern of maximum/minimum/maximum is similar to that of graphitic materials, however the third satellite peak (234 eV) is not as pronounced in the graphene oxide film.

7.4 Discussion

7.4.1 Appearance Threshold Energies of Cations

The proton desorption signal is the most prominent peak in the ESD-TOF mass spectrum of graphene oxide. In graphene oxide, hydrogen is bonded to several different functional groups. Consequently, H^+ may be produced from the breakage of a variety of R_1-C-H and R_2-O-H bonding sites, where R_1 is the methyl or phenyl substituent and R_2 is the carbonyl or phenyl substituent. The onset of desorption for H^+ occurs at 20 eV. Several ESD studies attribute the formation and desorption of H+ from hydrocarbons to the creation of states with two (or more) valence holes [75–77, 125]. For graphene oxide, the excitations leading to H^+ desorption can be attributed to an initial excitation of the C 2s level at $\sim$24 eV or the O 2s level at $\sim$22 eV. The closeness in proximity of the C 2s and O 2s levels make it difficult to determine from which bonding site H^+ is created from. Most likely, H^+ is produced form both O–H

and C–H sites.

An ESD study of condensed methanol also reported a similar threshold energy for H^+ at 20 ($\pm$1) eV [125]. Isotope substitution on the hydroxyl group of the methanol molecule revealed a strong preference for proton desorption from the methyl group over the hydroxyl group. However, the authors suggest the suppressions of H^+ desorption from hydroxyl groups is due to hydrogen bonding within the condensed methanol. The authors attribute the 20 eV threshold energy to an excitation localized on the $4a_1$ level of methanol, which is localized on the methyl group and strongly antibonding. However, for graphene oxide, localized molecular orbitals cannot be assigned, and therefore it is difficult to attribute from which bonding site H^+ originates.

The onset of desorption of the oxygen-containing fragments HCO^+ and $HCCO^+$ occurs at 19 eV. Similarly, the appearance threshold for the hydrocarbon fragments is at 20 eV. As with the proton desorption, the threshold energies of these cations is likely due to the formation of two-hole states localized on the C 2s shell.

7.4.2 Behavior of Cations as a Function of Electron Fluence

Since electron bombardment of surfaces is an important component of manufacturing, patterning, and imaging electronic devices, it is essential to investigate the manner in which a material such as graphene oxide will be affected by prolonged irradiation. In the previous section, it was reported that electron-stimulated desorption of cations was easily attained at electron energies as low as 20 eV. When the graphene oxide surface is irradiated with 50 eV electrons over a period of 60 minutes, the cation yields decay exponentially with increasing electron fluence. It should be noted that due to the presence of background water in UHV chamber, the H3O+ signal increases over the duration of the experiment.

The cross section for the electron-stimulated desorption of cations from graphene

oxide deposited on Si(100) was calculated from the data in Figure 7.5 from the equation described in Chapter 6. The cross sections for selected cations are listed in Table 7.1.

Table 7.1: Removal cross sections for cations emitted from ESD of graphene oxide deposited on Si(100) at 50 eV.

Ion	Cross section ($\times 10^{-19}$ cm^2)
H^+	1.93
HCO^+	1.49
$HCCO^+$	1.39
$CH_3{}^+$	1.22
$C_2H_3{}^+$	1.63

The effective cross section for cation removal from electron-stimulated desorption of the graphene oxide surface at 50 eV is $\sim 2 \times 10^{-19}$ cm^2.

7.5 Conclusions

Due to its chemical structure, facile synthesis, and simple deposition onto silicon substrates, graphene oxide is a promising precursor for the highly sought-after material graphene. ESD of graphene oxide results in the production and release of protons, hydroxonium ions, oxygenated functional groups, and hydrocarbon fragments. The onset of desorption for all desorbates occurs at 18–20 eV. From the threshold energies, cation production is attributed to excitations localized primarily on the C 2s. H^+ desorption may also have contributions from two-hole states localized at the O 2s valence shell. Cation yields decay exponentially as a function of increasing electron dose. Removal cross section values of 1–2×10^{-19} cm^2 indicated facile removal of protons and other functional groups from graphene oxide. However, post-irradiation

studies do not reveal graphene formation, or reduction of graphene oxide to graphene, due to low-energy electron bombardment.

CHAPTER VIII

CONCLUSION

The adsorption of hydrocarbons on silicon surfaces continues to be a subject of immense interest. The attention given to these systems is not only motivated by the potential technological applications, but is also driven by the important fundamental chemistry and physics surrounding these adsorbate-substrate systems. The impetus of the work outlined in this dissertation has been to bridge the gap between the fundamental and applied aspects associated with these surfaces.

The other common thread of the research presented here is the investigation of low-energy electron interactions with these surfaces. From the growth of large-scale carbon films to the detection of individual atoms and molecules on surfaces, low-energy electrons were employed to induce and to probe chemical and physical processes resulting from the interaction of these particles with hydrocarbon-covered silicon surfaces.

For the case of film growth, a low-temperature growth technique called electron beam chemical vapor deposition (EBCVD) was developed to deposit carbon films on Si(111) substrates in an effort to produce silicon carbide. It was shown that even at very low incident electron energies (8 eV) EBCVD is an effective method for removing hydrogen from acetylene overlayers.

Electron-stimulated desorption time-of-flight mass spectrometry measurements, in conjunction with resonance enhanced multiphoton ionization, confirmed the removal of hydrogen from acetylene chemisorbed on Si(111)-(7×7) and lead to the proposal of a mechanism for desorption. From the ESD studies, dissociative electron attachment resonances leading to the formation of neutral hydrogen were directly observed for acetylene chemisorbed on Si(111). This is the first reported study of this DEA

resonance from chemisorbed acetylene. All other studies involved the observation of DEA in gas phase [44] and condensed (physisorbed) [56, 74] acetylene.

Low-energy electrons were also used to explore surface reactions on graphene and graphene oxide. Graphene has garnered much interest in recent years due to its remarkable electronic properties. Electron-stimulated desorption of epitaxial graphene grown on SiC(0001) revealed that a significant amount of hydrogen is present on the surface of this material. Whether the source of the hydrogen is from the preparation of the SiC substrate or from the inherent hydrogen-termination of edge sites, the observation of desorbed hydrogen by ESD is important for understanding the electronic properties of graphene. Similar experiments were conducted on graphene oxide deposited on Si(100). Graphene oxide is a potential precursor material for graphene. Again, low-energy electron interactions proved to be important for both fundamental and applications-driven interests. From a fundamental chemistry perspective, ESD was utilized to gain insight into the chemical composition of graphene oxide. Currently, the exact chemical structure is unknown. ESD confirmed the presence of both unsaturated hydrocarbon fragments and oxygen-containing fragments in the form of HCO^+ and $HCCO^+$. From an applications outlook, continuous low-energy electron bombardment was used as a non-thermal, non-chemical method to reduce graphene oxide to graphene. Although electron irradiation resulted in the removal of oxygen-containing fragments, and left the graphene flakes in tact, there was no clear indication of graphene formation.

There are many investigations that can be conducted based on the groundwork laid by the work discussed in this thesis. For all of the adsorbate-substrate systems studied, the examination of neutral desorbates from ESD would be important supplementary information to expand upon and confirm the mechanisms proposed in Chapters 4–7. For the acetylene work, the REMPI detection of neutral acetylene would useful in gaining further understanding in the mechanism of $C_2D_2{}^+$ desorption.

The (3 + 1) REMPI of acetylene has been well established in the literature [127]. For epitaxial graphene and graphene oxide, the detection of neutral atomic and molecular hydrogen would be important measurements. For graphene oxide in particular, the time-of-flight distributions of neutral atomic hydrogen may help determine from which functional group hydrogen desorbs. Faster flight times may indicate removal of hydrogen from the hydroxyl groups in the basal plane, whereas slower flight times may indicate desorption from the terminal edge sites. Also, the detection of neutral CO is a very important measurement for this surface.

In conclusion, the interaction of low-energy electrons with hydrocarbons adsorbed on silicon surfaces has been investigated. Electron-stimulated desorption has been shown to be a useful tool, not only in fundamental investigations, but also when applied to film growth.

REFERENCES

[1] D. Li and R. B. Raner, "Materials science – graphene-based materials," *Science*, vol. 320, no. 5880, pp. 1170–1171, 2008.

[2] T. Seyller, A. Bostwick, K. V. Emtsev, K. Horn, L. Ley, J. L. McChesney, T. Ohta, J. D. Riley, E. Rotenberg, and F. Speck, "Epitaxial graphene: a new material," *Physica Status Solidi B*, vol. 245, no. 7, pp. 1436–1446, 2008.

[3] A. Itoh and H. Matsunami, "Single crystal growth of SiC and electronic devices," *Critical Reviews in Solid State Materials Sciences*, vol. 22, no. 2, pp. 111–197, 1997.

[4] P. Masri, "Silicon carbide and silicon carbide-based structures The physics of epitaxy," *Surface Science Reports*, vol. 48, no. 1-4, pp. 1–51, 2002.

[5] H. Matsunami and T. Kimoto, "Step-controlled epitaxial growth of SiC: High quality homoepitaxy," *Materials Science & Engineering R*, vol. 20, no. 3, pp. 125–166, 1997.

[6] M. Willander, M. Friesel, Q. U. L. Wahab, and B. Straumal, "Silicon carbide and diamond for high temperature device applications," *Journal of Materials Science: Materials in Electronics*, vol. 17, no. 1, pp. 1–25, 2006.

[7] O. Guise, H. Marbach, J. Levy, J. Ahner, and J. T. Yates, "Electron-beam-induced deposition of carbon films on Si(100) using chemisorbed ethylene as a precursor molecule," *Surface Science*, vol. 571, no. 1-3, pp. 128–138, 2004.

[8] S. J. Randolph, J. D. Fowlkes, and P. D. Rack, "Focused, nanoscale electron-beam-induced deposition and etching," *Critical Reviews in Solid State and Materials Sciences*, vol. 31, no. 3, pp. 55–89, 2006.

[9] N. Silvis-Cividjian and C. W. Hagen, "Electron-beam-induced nanometer-scale deposition," *Advances in Imaging and Electron Physics*, 2006.

[10] I. Utke, P. Hoffmann, and J. Melngailis, "Gas-assisted focused electron beam and ion beam processing and fabrication," *Journal of Vacuum Science & Technology B: Microelectronics and Nanometer Structures*, vol. 26, pp. 1197–1276, 2008.

[11] W. B. White, K. Rykaczewski, and A. G. Fedorov, "What controls deposition rate in electron-beam chemical vapor deposition?," *Physical Review Letters*, vol. 97, no. 8, pp. 086101–086104.

[12] K. R. Shepperd and T. M. Orlando unpublished results.

[13] C. D. Lane and T. M. Orlando, "Inelastic electron scattering and energy-selective negative ion reactions in molecular films on silicon surfaces," *Applied Surface Science*, vol. 253, no. 16, pp. 6646–6656, 2007.

[14] O. Ingólfsson, F. Weik, and E. Illenberger, "The reactivity of slow electrons with molecules at different degrees of aggregation: gas phase, clusters and condensed phase," *International Journal of Mass Spectrometry and Ion Processes*, vol. 155, no. 1-2, pp. 1–68, 1996.

[15] L. Christophorou and J. Olthoff, "Electron interactions with plasma processing gases: present status and future needs," *Applied Surface Science*, vol. 192, no. 1-4, pp. 309–326, 2002.

[16] A. Chutjian, A. Garscadden, and J. M. Wadehra, "Electron attachment to molecules at low electron energies," *Physics Reports-Review Section of Physics Letters*, vol. 264.

[17] L. Sanche, G. K., J. D. Brown, G. F. Rempfer, D. Roy, and M. Allan, "Interactions of low-energy electrons with atomic and molecular solids.," *Scanning Microscopy*, vol. 9, no. 3, pp. 619–656, 1995.

[18] I. Bald, J. Langer, P. Tegeder, and O. Ingólfsson, "From isolated molecules through clusters and condensates to the building blocks of life," *International Journal of Mass Spectrometry*, vol. 277, no. 1-3, pp. 4–25, 2008.

[19] R. D. Ramsier and J. T. Yates, "Electron-stimulated desorption: principles and applications," *Surface Science Reports*, vol. 12, no. 6, pp. 243–378, 1991.

[20] D. Menzel and R. Gomer, "Desorption from metal surfaces by low-energy electrons," *The Journal of Chemical Physics*, vol. 41, p. 3311, 1964.

[21] D. Menzel and R. Gomer, "Desorption from surfaces by slow-electron impact," *The Journal of Chemical Physics*, vol. 40, p. 1164, 1964.

[22] P. A. Redhead, "Interaction of slow electrons with chemisorbed oxygen," *Canadian Journal of Physics*, vol. 42, no. 5, pp. 886–905, 1964.

[23] A. E. Ennos, "The origin of specimen contamination in the electron microscope," *British Journal of Applied Physics*, vol. 4, pp. 101–106, 1953.

[24] W. F. van Dorp and C. W. Hagen, "A critical literature review of focused electron beam induced deposition," *Journal of Applied Physics*, vol. 104, p. 081301, 2008.

[25] C. D. Lane, K. R. Shepperd, A. B. Aleksandrov, and T. M. Orlando, "Electron stimulated desorption of cations from $SiCl_4$ multilayers adsorbed on Si(111)," *Surface Science*, vol. 593, no. 1-3, pp. 173–179, 2005.

[26] G. Mueller, "The Czochralski method – where we are 90 years after Jan Czochralski's invention.," *Crystal Research and Technology*, vol. 42, no. 12, pp. 1150–1161, 2007.

[27] J. A. Lely, "Darstellung von Einkristallen von Siliciumcarbid und Beherrschung von Art und Menge der eingebauten Verunreinigungen," *Angewandte Chemie*, vol. 66, p. 713, 1954.

[28] Y. M. Tairov and V. F. Tsvetkov, "Investigation of growth processes of ingots of silicon carbide single crystals," *Journal of Crystal Growth*, vol. 43, no. 2, pp. 209–212, 1978.

[29] Y. M. Tairov and V. F. Tsvetkov, "General principles of growing large-size single crystals of various silicon carbide polytypes," *Journal of Crystal Growth*, vol. 52, pp. 146–150, 1981.

[30] S. Nishino, J. A. Powell, and H. A. Will, "Production of large-area single-crystal wafers of cubic SiC for semiconductor devices," *Applied Physics Letters*, vol. 42, pp. 460–462, 1983.

[31] V. M. Bermudez, "Structure and properties of cubic silicon carbide (100) surfaces: a review," *Physica Status Solidi B*, vol. 202, no. 1, 1997.

[32] J. Schlichting, "Chemical vapor deposition of silicon carbide," *Powder Metallurgy International*, vol. 12.

[33] K. Shibahara, S. Nishino, and H. Matsunami, "Antiphase-domain-free growth of cubic SiC on Si(100)," *Applied Physics Letters*, vol. 50, pp. 1888–1890, 1987.

[34] M. De Crescenzi, M. Marucci, R. Gunnella, P. Castrucci, M. Casalboni, and R. F. Dufour, G., "$Si_{1-x}C_x$ formation by reaction of Si(111) with acetylene: growth mode, electronic structure and luminescence investigation," *Surface Science*, vol. 426, no. 3, pp. 277–289, 1999.

[35] M. Salmerón and A. Baró, "Experimental observation of chemical shifts in auger spectrum from surface layers of SiO_2 during electron bombardment," *Surface Science*, vol. 29, no. 1, pp. 300–302, 1972.

[36] E. G. Keim, "Si-O bond formation on the Si(100)- 2×1 surface at the early stage of oxidation as observed by AES," *Surface Science*, vol. 148, no. 2-3, pp. 641–644, 1984.

[37] L. Calliari, "AES and core level photoemission in the study of aC and aC: H," *Diamond & Related Materials*, vol. 14, no. 8, pp. 1232–1240, 2005.

[38] L. Calliari, G. Speranza, J. C. Lascovich, and A. Santoni, "The graphite core-valence-valence Auger spectrum," *Surface Science*, vol. 501, no. 3, pp. 253–260, 2002.

[39] L. Calliari, G. Speranza, and A. Santoni, "The graphite Valence Band electronic structure: a combined Core–Valence–Valence Auger and Valence Band photoemission study," *Journal of Electron Spectroscopy and Related Phenomena*, vol. 127, no. 1-2, pp. 125–130, 2002.

[40] J. T. Grant and T. W. Haas, "Identification of the form of carbon at a Si(100) surface using auger electron spectroscopy," *Physics Letters A*, vol. 33, no. 6, p. 386, 1970.

[41] J. T. Grant and T. W. Haas, "Auger electron spectroscopy studies of carbon overlayers on metal surfaces," *Surface Science*, vol. 24, no. 1, pp. 332–334, 1971.

[42] T. W. Haas, J. T. Grant, and G. J. Dooley III, "Chemical effects in Auger electron spectroscopy," *Journal of Applied Physics*, vol. 43, p. 1853, 1972.

[43] G. Speranza, L. Calliari, N. Laidani, and M. Anderle, "Semi-quantitative description of C hybridization via s-and p-partial density of states probing: an electron spectroscopy study," *Diamond & Related Materials*, vol. 9, no. 11, pp. 1856–1861, 2000.

[44] R. Dressler and M. Allan, "A dissociative electron attachment, electron transmission, and electron energy-loss study of the temporary negative ion of acetylene," *The Journal of Chemical Physics*, vol. 87, pp. 4510–4518, 1987.

[45] C. C. Cheng, P. A. Taylor, R. M. Wallace, H. Gutleben, and M. L. Clemen, "Hydrocarbon surface chemistry on Si(100)," *Thin Solid Films*.

[46] F. Tao and G. Q. Xu, "Attachment chemistry of organic molecules on Si(111)-7× 7," *Accounts of Chemical Research*, vol. 37, no. 11, pp. 882–893, 2004.

[47] P. Castrucci, A. Sgarlata, M. Scarselli, and M. De Crescenzi, "STM study of acetylene reaction with Si(111): observation of a carbon-induced Si(111) $\sqrt{3} \times \sqrt{3}$ R 30 ° reconstruction," *Surface Science*, vol. 531, no. 1, pp. 329–334, 2003.

[48] M. De Crescenzi, R. Bernardini, S. Pollano, R. Gunnella, P. Castrucci, G. Dufour, and F. Rochet, "Acetylene on Si(111): carbon incorporation in the growth of c-SiC thin layers," *Surface Science*, vol. 489, no. 1-3, pp. 185–190, 2001.

[49] V. De Renzi, R. Biagi, and U. del Pennino, "Temperature dependence of acetylene adsorption and reaction on Si(111)-(7×7)," *Applied Surface Science*, vol. 184, no. 1-4, pp. 90–95, 2001.

[50] V. De Renzi, R. Biagi, and U. del Pennino, "Acetylene adsorption on the Si(111)-(7× 7) surface: ultraviolet photoemission and high-resolution electron-energy-loss spectroscopies," *Physical Review B*, vol. 64, p. 155305, 1999.

[51] K. Takayanagi, Y. Tanishiro, M. Takahashi, and S. Takahashi, "Structural-analysis of Si(111)-7×7 by UHV-transmission electron-diffraction and microscopy," *Journal of Vacuum Science & Technology A*, vol. 3, no. 3, pp. 1502–1506, 1985.

[52] J. Yoshinobu, D. Fukushi, M. Uda, E. Nomura, and M. Aono, "Acetylene adsorption on Si(111)(7×7): A scanning-tunneling-microscopy study.," *Physical Review. B, Condensed Matter*, vol. 46, no. 15, p. 9520, 1992.

[53] J. Yoshinobu, H. Tsuda, M. Onchi, and M. Nishijima, "Rehybridization of acetylene on the Si(111)(7×7) surface: a vibrational study," *Chemical Physics Letters*, vol. 130, no. 3, pp. 170–174, 1986.

[54] R. J. Hamers, R. M. Tromp, and J. E. Demuth, "Surface electronic structure of Si(111)-(7×7) resolved in real space," *Physical Review Letters*, vol. 56, no. 18, pp. 1972–1975, 1986.

[55] P. A. Taylor, R. M. Wallace, C. C. Cheng, W. H. Weinberg, and M. J. Dresser, "Adsorption and decomposition of acetylene on Si(100)-(2×1)," *Journal of the American Chemical Society*, vol. 114, pp. 6754–6760, 1991.

[56] P. Możejko, A. D. Bass, L. Parenteau, and L. Sanche, "Intrinsic and extrinsic factors in anion electron-stimulated desorption: D^- from deuterated hydrocarbons condensed on Kr and water ice films," *Journal of Chemical Physics*, vol. 121, p. 10181, 2004.

[57] F. Rochet, G. Dufour, P. Prieto, F. Sirotti, and F. C. Stedile, "Electronic structure of acetylene on Si(111)-7×7: X-ray photoelectron and x-ray absorption spectroscopy," *Physical Review B*, vol. 57, no. 11, pp. 6738–6748, 1998.

[58] R. G. Cavell and D. A. Allison, "Photoelectron spectra of acetylene with He^I, He^{II}, Zr Mζ, and Mg Kα radiation sources," *Journal of Chemical Physics*, vol. 69, no. 1, pp. 159–166, 1978.

[59] J. H. Fock and E. E. Koch, "Partial cross sections and autoionization resonances in the valence-shell photoemission from solid acetylene," *Chemical Physics Letters*, vol. 105, no. 1, pp. 38–43, 1984.

[60] J. H. Fock, H. J. Lau, and E. E. Koch, "Electronic band structure of solid CO_2 as determined from the hν-dependence of photoelectron emission," *Chemical Physics*, vol. 83, no. 3, pp. 377–389, 1984.

[61] F. Rochet, G. Dufour, F. Stedile, F. Sirotti, P. Prieto, and M. De Crescenzi, "Acetylene gas as a carbon source: An x-ray photoemission spectroscopy and near-edge x-ray absorption fine structure spectroscopy study of its stability on Si(111)-7×7," *Journal of Vacuum Science and Technology B-Microelectronics Nanometer Structure*, vol. 16, no. 3, pp. 1692–1696, 1998.

[62] J. E. Rowe and H. Ibach, "Surface and bulk contributions to ultraviolet photoemission spectra of silicon," *Physical Review Letters*, vol. 32, no. 8, pp. 421–424, 1974.

[63] J. T. Tate, P. T. Smith, and A. L. Vaughan, "A Mass Spectrum Analysis of the Products of Ionization by Electron Impact in Nitrogen, Acetylene, Nitric Oxide, Cyanogen and Carbon Monoxide," *Physical Review*, vol. 48, no. 6, pp. 525–531, 1935.

[64] C. E. Brion, "The Franck-Condon principle and the ionization of acetylene by electron impact," *Chemical Physics Letters*, vol. 3, no. 1, 1969.

[65] F. P. Lossing, "Threshold ionization of acetylene by monoenergetic electron impact," *International Journal of Mass Spectrometry and Ion Physics*, vol. 5, no. 3-4, pp. 190–192, 1970.

[66] E. H. van Veen and F. L. Plantenga, "Low-energy electron-impact excitation spectra of acetylene," *Chemical Physics Letters*, vol. 38, no. 3, pp. 493–497, 1976.

[67] M. Davister and R. Locht, "The dissociative electroionization of C_2H_2, C_2D_2 and C_2HD. Investigation of the $(C_2H(D))(+)$ and $(H(D))(+)$ dissociation channels. The $(D)H–C_2H(D)$ binding energy," *Chemical Physics (ISSN 0301-0104)*, vol. 189, no. 3, pp. 805–824, 1994.

[68] M. Davister and R. Locht, "The dissociative ionization of C_2H_2 and C_2D_2. The $[CH(CD)]^+$ dissociation channel. The $H(D)C–C(D)H$ binding energy," *Chemical Physics*, vol. 191, no. 1-3, pp. 333–346, 1995.

[69] R. Locht and M. Davister, "The dissociative ionization of C_2H_2. The C^+, $C_2{}^+$ and $CH_2{}^+$ dissociation channels. The vinylidene ion as a transient?," *Chemical Physics*, vol. 195, no. 1-3, pp. 443–456, 1995.

[70] S. Zheng and S. Srivastava, "Electron-impact ionization and dissociative ionization of acetylene," *Journal of Physics B: Atomic, Molecular, and Optical Physics*, vol. 29, no. 14, pp. 3235–3244, 1996.

[71] S. Feil, K. Głuch, A. Bacher, S. Matt-Leubner, D. K. Böhme, P. Scheier, and T. D. Märk, "Cross sections and ion kinetic energy analysis for the electron impact ionization of acetylene," *Journal of Chemical Physics*, vol. 124, no. 21, p. 214307, 2006.

[72] Y. K. Kim, M. A. Ali, and M. E. Rudd, "Electron-impact total ionization cross sections of CH and C_2H_2," *Journal of Research of the National Institute of Standards and Technology*, vol. 102, no. 6, pp. 693–696, 1997.

[73] S. J. King and S. D. Price, "Electron ionization of acetylene," *Journal of Chemical Physics*, vol. 127, p. 174307, 2007.

[74] P. Możejko, L. Parenteau, A. D. Bass, and L. Sanche, "D^- ion desorption from condensed CD_4, C_2D_2, C_2D_4, C_2D_6 and C_3D_8 molecules induced by electron impact," *Radiation Physics and Chemistry*, vol. 68, no. 1-2, pp. 215–219, 2003.

[75] J. A. Kelber and M. L. Knotek, "Electron stimulated desorption of condensed, branched alkanes," *Surface Science*, vol. 121, no. 1, pp. 499–506, 1982.

[76] J. A. Kelber and M. L. Knotek, "Electron-stimulated desorption in organic molecular solids," *Journal of Vacuum Science & Technology A: Vacuum, Surfaces, and Films*, vol. 1, no. 2, pp. 1149–1153, 1983.

[77] J. A. Kelber and M. L. Knotek, "Electron-stimulated desorption from partially fluorinated hydrocarbon thin films: Molecules with common versus separate hydrogen and fluorine bonding sites," *Physical Review B*, vol. 30, no. 1, pp. 400–403, 1984.

[78] V. M. Bermudez, T. M. Parrill, and R. Kaplan, "Electron-stimulated desorption of positive ions from hexagonal α-SiC," *Surface Science*, vol. 173, no. 1, pp. 234–244, 1986.

[79] N. G. Petrik, K. Knutsen, E. Paparazzo, S. Lea, D. M. Camaioni, and T. M. Orlandos, "Electron beam induced damage of $NaNO_3$ single crystals: An energy, temperature, and quantum state resolved study," *Journal of Physical Chemistry B*, vol. 104, no. 7, pp. 1563–1571, 2000.

[80] D. F. Dance and I. C. Walker, "Threshold electron energy-loss spectra for some simple alkynes," *Journal of the Chemical Society, Faraday Transactions II*, vol. 70, pp. 1426–1434, 1974.

[81] P. Plessis and P. Marmet, "Electroionization study of acetylene and fragment ions," *International Journal of Mass Spectrometry and Ion Processes*, vol. 70, no. 1, pp. 23–44, 1986.

[82] H. W. Kroto, J. R. Heath, S. C. O'Brien, R. F. Curl, and R. E. Smalley, "C60: Buckminsterfullerene," *Nature*, vol. 318, pp. 162–163, 1985.

[83] S. Ijima, "Helical microtubulus of graphitic carbon," *Nature*, vol. 354, pp. 56–58, 1991.

[84] K. S. Novoselov, A. K. Geim, S. V. Morozov, D. Jiang, Y. Zhang, S. V. Dubonos, I. V. Grigorieva, and A. A. Firsov, "Electric field effect in atomically thin carbon films," 2004.

[85] A. K. Geim and K. S. Novoselov, "The rise of graphene," *Nature Materials*, vol. 6, no. 3, pp. 183–191, 2007.

[86] K. S. Kim, Y. Zhao, H. Jang, S. Y. Lee, J. M. Kim, K. S. Kim, J. H. Ahn, P. Kim, J. Y. Choi, and B. H. Hong, "Large-scale pattern growth of graphene films for stretchable transparent electrodes," *Nature*, vol. 457, pp. 706–710, 2009.

[87] H. Kang, A. Kulkarni, S. Stankovich, R. S. Ruoff, and S. Baik, "Restoring electrical conductivity of dielectrophoretically assembled graphite oxide sheets by thermal and chemical reduction techniques," *Carbon*, vol. 47, pp. 1520–1525.

[88] H. C. Schniepp, J. L. Li, M. J. McAllister, H. Sai, M. Herrera-Alonso, D. H. Adamson, R. K. Prud'homme, R. Car, D. A. Saville, and I. A. Aksay, "Functionalized single graphene sheets derived from splitting graphite oxide," *Journal of Physical Chemistry B-Condensed Phase*, vol. 110, no. 17, pp. 8535–8539, 2006.

[89] S. Stankovich, D. A. Dikin, R. D. Piner, K. A. Kohlhaas, A. Kleinhammes, Y. Jia, Y. Wu, S. B. T. Nguyen, and R. S. Ruoff, "Synthesis of graphene-based nanosheets via chemical reduction of exfoliated graphite oxide," *Carbon*, vol. 45, no. 7, pp. 1558–1565, 2007.

[90] C. Berger, Z. Song, T. Li, X. Li, A. Y. Ogbazghi, R. Feng, Z. Dai, A. N. Marchenkov, E. H. Conrad, and W. A. de Heer, "Ultrathin Epitaxial Graphite: 2D Electron Gas Properties and a Route toward Graphene-based Nanoelectronics," *J. Phys. Chem. B*, vol. 108, no. 52, pp. 19912–19916, 2004.

[91] J. Hass, W. A. de Heer, and E. H. Conrad, "The growth and morphology of epitaxial multilayer graphene," *Journal of Physics: Condensed Matter*, vol. 20, p. 323202, 2008.

[92] M. Knotek and J. Houston, "Study of the stepwise oxidation and nitridation of Si (111): Electron stimulated desorption, Auger spectroscopy, and electron loss spectroscopy," *Journal of Vacuum Science & Technology B: Microelectronics and Nanometer Structures*, vol. 1, no. 4, pp. 899–914, 1983.

[93] C. Berger, Z. Song, X. Li, X. Wu, N. Brown, C. Naud, D. Mayou, T. Li, J. Hass, A. N. Marchenkov, E. H. Conrad, P. N. First, and W. A. de Heer, "Electronic confinement and coherence in patterned epitaxial graphene," *Science*, vol. 312, no. 5777, pp. 1191–1196, 2006.

[94] B. C. Brodie, "On the atomic weight of graphite," *Philosophical Transactions of the Royal Society of London*, pp. 249–259, 1859.

[95] W. S. Hummers and R. E. Offeman, "Preparation of graphitic oxide," *Journal of the American Chemical Society*, vol. 80, no. 6, pp. 1339–1339, 1958.

[96] D. W. Boukhvalov and M. I. Katsnelson, "Modeling of graphite oxide," *Journal of the American Chemical Society*, vol. 130, no. 32, pp. 10697–10701, 2008.

[97] R. Lahaye, H. K. Jeong, C. Y. Park, and Y. H. Lee, "Density functional theory study of graphite oxide for different oxidation levels," *Physical Review B*, vol. 79, p. 125435, 2009.

[98] R. J. Beckett and R. C. Croft, "The Structure of graphite oxide," *The Journal of Physical Chemistry*, vol. 56, no. 8, pp. 929–935, 1952.

[99] W. Cai, R. D. Piner, F. J. Stadermann, S. Park, M. A. Shaibat, Y. Ishii, D. Yang, A. Velamakanni, S. J. An, and M. Stoller, "Synthesis and solid-state NMR structural characterization of ^{1}3C-labeled graphite oxide," *Science*, vol. 321, no. 5897, p. 1815, 2008.

[100] H. Y. He, T. Riedl, A. Lerf, and J. Klinowski, "Solid-state nmr studies of the structure of graphite oxide," *Jounal of Physical Chemistry*.

[101] G. Hristea and C. Panaitescu, "Structural aspects about graphite oxides," *Revue Roumaine de Chimie*, vol. 46, pp. 1107–1111, 2001.

[102] H. K. Jeong, H. J. Noh, J. Y. Kim, M. H. Jin, C. Y. Park, and Y. H. Lee, "X-ray absorption spectroscopy of graphite oxide," *European Physics Letters*.

[103] A. Lerf, H. He, M. Forster, and J. Klinowski, "Structure of Graphite Oxide Revisited?," *Journal of Physical Chemistry B*, vol. 102, no. 23, pp. 4477–4482, 1998.

[104] M. Mermoux, Y. Chabre, and A. Rousseau, "FTIR and ^{1}3C NMR study of graphite oxide," *Carbon*, vol. 29, no. 3, pp. 469–474, 1991.

[105] K. A. Mkhoyan, A. W. Contryman, J. Silcox, D. A. Stewart, G. Eda, C. Mattevi, S. Miller, and M. Chhowalla, "Atomic and electronic structure of graphene-oxide," *Nano Letters*, vol. 9, no. 3, pp. 1058–1063, 2009.

[106] T. Nakajima, A. Mabuchi, and R. Hagiwara, "A new structure of graphite oxide," *Carbon*, vol. 26, no. 3, pp. 357–361, 1988.

[107] T. Nakajima and Y. Matsuo, "Formation process and structure of graphite oxide," *Carbon(New York, NY)*, vol. 32, no. 3, pp. 469–475, 1994.

[108] T. Szabo, O. Berkesi, P. Forgo, K. Josepovits, Y. Sanakis, D. Petridis, and I. Dekany, "Evolution of surface functional groups in a series of progressively oxidized graphite oxides," *Chemistry of Materials*, vol. 18, no. 11, pp. 2740–2749, 2006.

[109] L. J. Cote, F. Kim, and J. Huang, "Langmuir- Blodgett Assembly of Graphite Oxide Single Layers," *Journal of the American Chemical Society*, vol. 131, no. 3, pp. 1043–1049, 2008.

[110] H. A. Becerril, J. Mao, Z. Liu, R. M. Stoltenberg, Z. Bao, and Y. Chen, "Evaluation of solution-processed reduced graphene oxide films as transparent conductors," *ACS Nano*, vol. 2, no. 3, pp. 463–470, 2008.

[111] H. K. Jeong, Y. P. Lee, M. H. Jin, E. S. Kim, J. J. Bae, and Y. H. Lee, "Thermal stability of graphite oxide," *Chemical Physics Letters*, vol. 470, pp. 255–258, 2009.

[112] I. Jung, D. A. Dikin, R. D. Piner, and R. S. Ruoff, "Tunable electrical conductivity of individual graphene oxide sheets reduced at low temperatures," *Nano Letters*, vol. 8, no. 12, pp. 4283–4287, 2008.

[113] M. J. McAllister, J. L. Li, D. H. Adamson, H. C. Schniepp, A. A. Abdala, J. Liu, M. Herrera-Alonso, D. L. Milius, R. Car, R. K. Prud'homme, and I. A. Aksay, "Single sheet functionalized graphene by oxidation and thermal expansion of graphite," *Chemistry of Materials*, vol. 19, pp. 4396–4404, 2007.

[114] A. B. Bourlinos, D. Gournis, D. Petridis, T. Szabo, A. Szeri, and I. Dekany, "Graphite oxide: chemical reduction to graphite and surface modification with primary aliphatic amines and amino acids," *Langmuir*, vol. 19, no. 15, pp. 6050–6055, 2003.

[115] S. Gilje, S. Han, M. Wang, K. L. Wang, and R. B. Kaner, "A chemical route to graphene for device applications," *Nano Letters*, vol. 7, no. 11, pp. 3394–3398, 2007.

[116] C. Gómez-Navarro, M. Burghard, and K. Kern, "Elastic properties of chemically derived single graphene sheets," *Nano Letters*, vol. 8, no. 7, pp. 2045–2049, 2008.

[117] C. Gómez-Navarro, R. T. Weitz, A. M. Bittner, M. Scolari, A. Mews, M. Burghard, and K. Kern, "Electronic transport properties of individual chemically reduced graphene oxide sheets," *Nano Letters*, vol. 7, no. 11, pp. 3499–3503, 2007.

[118] Z. Luo, P. M. Vora, E. J. Mele, A. T. C. Johnson, and J. M. Kikkawa, "Photoluminescence and band gap modulation in graphene oxide," *Applied Physics Letters*, vol. 94, p. 111909, 2009.

[119] J. T. Robinson, F. K. Perkins, E. S. Snow, Z. Wei, and P. E. Sheehan, "Reduced graphene oxide molecular sensors," *Nano Letters*, vol. 8, no. 10, pp. 3137–3140, 2008.

[120] V. C. Tung, M. J. Allen, Y. Yang, and R. B. Kaner, "High-throughput solution processing of large-scale graphene," *Nature Nanotechnology*, 2008.

[121] G. Wang, J. Yang, J. Park, X. Gou, B. Wang, H. Liu, and J. Yao, "Facile synthesis and characterization of graphene nanosheets," *Journal of Physical Chemistry C*, vol. 112, no. 22, pp. 8192–8195, 2008.

[122] D. Yang, A. Velamakanni, G. Bozoklu, S. Park, M. Stoller, R. D. Piner, S. Stankovich, I. Jung, D. A. Field, and C. A. Ventrice, "Chemical analysis of graphene oxide films after heat and chemical treatments by X-ray photoelectron and Micro-Raman spectroscopy," *Carbon*, vol. 47, no. 1, pp. 145–152, 2009.

[123] A. K. Bhattacharya and M. A. Chesters, "The adsorption and decomposition of methanol on Fe(110) studied by Auger electron spectroscopy," *Journal of Catalysis*, vol. 109, no. 2, pp. 314–319, 1988.

[124] R. R. Rye, T. E. Madey, J. E. Houston, and P. H. Holloway, "Chemical-state effects in Auger electron spectroscopy," *Journal of Chemical Physics*, vol. 69, pp. 1504–1512, 1978.

[125] R. Stockbauer, E. Bertel, and T. E. Madey, "The origin of H^+ in electron-stimulated desorption of condensed CH_3OH," *Journal of Chemical Physics*, vol. 76, pp. 5639–5641, 1982.

[126] S. Y. Chu and A. B. Anderson, "Acetylene adsorption on Si(111): Molecular orbital theory," *Surface Science*, vol. 194, no. 1-2, pp. 55–62, 1988.

[127] T. M. Orlando, S. L. Anderson, J. R. Appling, and M. G. White, "MPI photoelectron spectroscopy of ungerade excited states of acetylene: Intermediate state mixing and ion state selection," *Journal of Chemical Physics*, vol. 87, p. 852, 1987.